Enzyme-Driven Phase Separation

Enzyme-Driven Phase Separation

Damiano Andreghetti,[1,2] Alfredo Braunstein,[1,3,2] Luca Dall'Asta,[1,2,3] and Andrea Gamba[1,2,3,*]
[1]*Institute of Condensed Matter Physics and Complex Systems, Department of Applied Science and Technology, Politecnico di Torino, Corso Duca degli Abruzzi 24, 10129 Torino, Italy*
[2]*Istituto Nazionale di Fisica Nucleare (INFN), Via Pietro Giuria 1, 10125 Torino, Italy*
[3]*Italian Institute for Genomic Medicine, Candiolo Cancer Institute, Fondazione del Piemonte per l'Oncologia (FPO), Candiolo, 10060 Torino, Italy*

(Received 7 December 2025; accepted 12 June 2026; published 14 July 2026)

The formation of polarized signaling domains on cell membranes is a fundamental example of biological pattern formation. While such patterns resemble structures from equilibrium phase separation, they are intrinsically nonequilibrium, driven by energy-consuming enzymatic cycles that switch molecules like phosphoinositides or small GTPases between distinct states. Here, we develop a minimal model of this enzyme-driven phase-ordering process. Starting from microscopic reaction kinetics, we derive a mesoscopic theory that belongs to the class of active model A with a global constraint. This framework yields an explicit mean-field phase diagram and closed-form expressions for key observables, such as interfacial tension, domain fractions, and phase-coexistence boundaries, in terms of kinetic rates. In this context, phase coexistence is controlled by nonequilibrium parameters such as- catalytic rates and enzymatic asymmetry, rather than equilibrium parameters such as saturation concentrations. The resulting phase-separated domains rapidly exchange material with their surroundings. Their maintenance requires a continuous power input determined by enzymatic kinetics. The predicted phenomenology is consistent with experimental observations on reconstituted systems of phosphoinositide and Rab5 membrane patterning. We further study how metastable uniform states decay via nucleation of minority-phase domains and subsequent coarsening, driven by an effective interfacial tension. Using largedeviation theory, we derive the critical nucleation radius under the action of the intrinsic, multiplicative chemical noise. The analytical results are quantitatively confirmed by stochastic simulations of the process. Our work provides a theoretical framework identifying key biochemical parameters controlling active phase separation on membrane scaffolds, offering testable predictions for experiments.

DOI: 10.1103/jmcc-mvrs

I. INTRODUCTION

Eukaryotic cells display a remarkable degree of spatial organization, with a diverse array of supramolecular structures, from organelles to specialized membrane domains, that underpin essential functions such as locomotion, signaling, and division [1]. Understanding the physical principles that guide the formation and maintenance of these dynamic structures remains a central challenge at the interface of biology and physics. Phase separation has been proposed as a unifying concept, capable of explaining the localization of molecular factors and the formation of biological condensates [2,3]. Initially, this concept was formed by drawing analogies from the physics of quasiequilibrium "passive" phase separation in polymer solutions and colloidal suspensions, where demixing is driven by a system's relaxation toward thermodynamic equilibrium, through the minimization of its free energy. However, biological self-organization is an inherently nonequilibrium process, often driven by energy-consuming, enzymatically controlled processes that are highly specific [4–6]. These active mechanisms can lead to distinct phenomenologies, such as the suppression of coarsening and novel growth kinetics [7–11], necessitating theoretical frameworks that go beyond classical equilibrium thermodynamics [7,8,10,12–20].

A canonical example of such active organization is the phase ordering of membrane-residing signaling molecules, such as phosphoinositides or small GTPases [21–23], into signaling domains. Critically, these spatial patterns do not arise from passive equilibrium interactions but are driven by energy-dissipating enzymatic cycles. Feedback loops, whether direct or mediated by ancillary factors, promote the colocalization of enzymes with their reaction products, thereby establishing a self-reinforcing cycle. This leads to a phenomenon that resembles classical phase separation: the formation of distinct spatial domains enriched in a specific molecular state (e.g., GTP bound or phosphorylated). However, the underlying mechanism is fundamentally different, as it is sustained by continuous, energy-consuming interconversion between states. Consequently, blocking the required

*Contact author: andrea.gamba@polito.it

energy supply (e.g., by removing ATP) leads to the dissolution of domains, demonstrating that the system is maintained far from thermodynamic equilibrium [21].

In this work, we develop a minimal model of this enzyme-driven phase-ordering process. We start from microscopic enzymatic kinetics and derive a mesoscopic theory that captures the system's essential features. The theory is characterized by a nonconserved order parameter coupled to a global constraint on molecular species fractions, which provides the stabilizing mechanism that makes phase coexistence possible [24–29]. The resulting dynamics is thus in the class of an active version of model A with a globally conserved field [30,31]. In this context, it is worth recalling that the mapping of reaction-diffusion systems to Hohenberg-Halperin dynamical universality classes [30] has deep roots. Already in the 1970s, the Schlögl model had demonstrated how chemical reactions could produce first-order phase transitions, controlled by an effective bistable potential [32]. Later, Goldbeter and Koshland highlighted the emergence of switchlike behavior and bistability in systems governed by antagonistic enzymes [33]. Such chemical reaction schemes typically lack a locally conserved order parameter, as chemical factors can be freely converted into each other. They thus tend to exhibit model A–type dynamics, where phase-separated patterns disappear through coarsening (the progressive elimination of finer structures as larger ones grow) [34]. However, when reaction-diffusion systems are subject to global constraints, stable coexistence of phases is possible. This principle is crucial in mass-conserving reaction-diffusion theories of membrane polarization where shuttling of enzymes between the membrane and a fast-diffusing cytosolic reservoir induce model A dynamics with global conservation of an order parameter: here, coarsening drives the system toward the stable coexistence of competing phases [24,25,35,36]. Importantly, in this scheme, phase-separated domains emerge not only via spontaneous linear instabilities of the Turing type but also via the potentially more controllable process of homogeneous or heterogeneous nucleation from a uniform metastable phase [24,25,35–37]. Similar models have been proposed to explain the formation of polarity patterns in different biological systems [26,38–40] and are emerging as a general paradigm for intracellular pattern formation [28,35,41,42]. The study of the level sets of conserved quantities (reactive phase spaces) and submanifolds of reactive equilibria (reactive nullclines) of mass-conserving systems has unraveled nontrivial mechanisms of wavelength selection and pattern stability in these nonequilibrium settings [27,29,42,43]. Depending on the structure of the underlying reaction network, such systems can exhibit features of either model A or model B dynamics, where model B is characterized by the added constraint of local mass conservation [42,43]. For systems that are microscopically active due to energy consumption, coarse graining is expected to yield "active" versions of the Hohenberg-Halperin classes. For instance, an active modification of model B including terms that explicitly break detailed balance has been successfully applied to the study of motility-induced phase separation [6,16,44,45]. In general, the derivation of mesoscopic theories from microscopic kinetics remains an open challenge [46]. Here we address this point by showing how underlying enzymatic cycles lead naturally to an active model A dynamics subject to a global constraint. In this framework, the nonequilibrium nature of the system is captured through the kinetic nonlinearities and the global coupling to a reservoir, providing a direct link between biochemical energy dissipation and stable phase coexistence. This formulation, while incorporating realistic ingredients such as local feedback and rapid exchange with the reservoir, remains analytically tractable. Within a mean-field approximation, we obtain an explicit phase diagram and closed-form expressions for key observables, including interfacial tension and phase-coexistence boundaries, directly in terms of basic kinetic rates. This allows us to identify how phase coexistence is promoted by enzyme affinity and catalytic asymmetries, and to determine the interfacial properties and energy dissipation required to sustain the active domains. The predictions of this analytical framework are confirmed by numerical simulations of a lattice-gas implementation of the full stochastic process. Moving beyond mean-field theory, we then analytically investigate fluctuation-driven events, deriving an explicit expression for the critical nucleation radius that quantifies the stochastic transition to a phase-separated state. Our results provide a theoretical foundation for interpreting experiments and identifying the key biochemical parameters that control active phase separation on membranes.

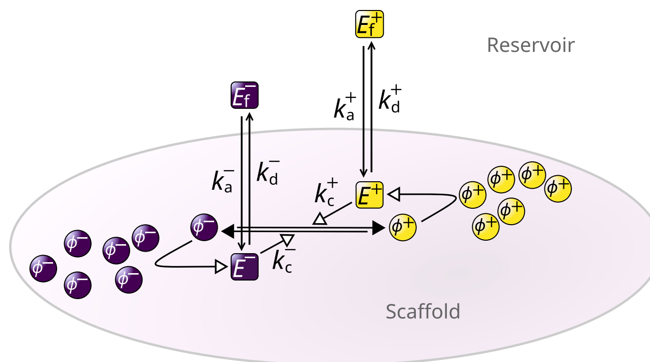

FIG. 1. Schematic representation of the model reaction network. The scaffold (e.g., a lipid membrane) is populated by two molecular species, ϕ^+ and ϕ^-, which can be converted into one another (horizontal arrows). This conversion process is catalyzed (oblique arrows) by scaffold-bound enzymes, $E^\pm$, with catalytic rates $k_c^\pm$. Their free forms, $E_f^\pm$, diffuse in a reservoir (e.g., the cytosol), binding to the scaffold with rates $k_a^\pm$ and unbinding with rates $k_d^\pm$ (vertical arrows). The enzymes preferentially bind where the concentration of their respective product molecules (i.e., $\phi^\pm$) is higher, creating a self-reinforcing feedback loop (curved arrows). See Tables I and II for a summary of the relevant fields and parameters.

II. STOCHASTIC MODEL

We consider a minimal model for bistable molecular switches on a slow-diffusion scaffold (typically, a membrane), inspired by canonical signaling systems involving phosphoinositides or small GTPases, where antagonistic enzymes regulate substrate states [47,48]. The model (Fig. 1) comprises two-state molecules $\phi^\pm$ that diffuse on the scaffold with diffusivity D. Their interconversion is catalyzed by enzymes $E^{\pm}$:

$$E^{\pm} + \phi^{\mp} \xrightarrow{k_c^{\pm}} E^{\pm} + \phi^{\pm}. \tag{1}$$

We assume the enzymes operate via Michaelis-Menten kinetics with constants $K_m^{\pm}$, thus allowing for both linear and saturation regimes in the reaction rates. The enzymes also diffuse on the scaffold with diffusivity D. Furthermore, they shuttle between a fast-diffusing reservoir (typically the cytosol, with diffusivity $D_f \gg D$), and the slow-diffusing scaffold, preferentially binding to scaffold regions enriched in their corresponding product $\phi^{\pm}$:

$$E_f^{\pm} + \phi^{\pm} \xrightarrow{k_a^{\pm}} E^{\pm} + \phi^{\pm}, \tag{2a}$$

$$E^{\pm} \xrightarrow{k_d^{\pm}} E_f^{\pm}. \tag{2b}$$

Here, $E_f^{\pm}$ and $E^{\pm}$ denote the free and scaffold-bound forms of the enzymes, respectively. This feedback, where product recruits its own producer, provides a core mechanism for phase separation. We also allow for a small, basal first-order conversion:

$$\phi^{\mp} \xrightarrow{k_b^{\pm}} \phi^{\pm}. \tag{3}$$

This reaction provides a background transition rate independent of enzymatic feedback.

The above-described reaction-diffusion process involves multiple scales and a very large number of degrees of freedom (see Appendix A). As a consequence, integration of the corresponding master equation is unfeasible. To make this problem tractable, we derive from the microscopic reaction rules, Eqs. (1)–(3), mesoscopic Langevin equations for a vector $\vec{X} = (\phi^+, \phi^-, E^+, E^-, E_f^+, E_f^-)$ of coarse-grained concentration fields, incorporating fluctuations consistent with the central limit theorem (see Appendix B and Ref. [49]):

$$\partial_t \vec{X}(\vec{x}, t) = \vec{F}[\vec{X}(\vec{x}, t)] + \vec{\Xi}(\vec{x}, t),$$

where $\vec{x}$ is a spatial coordinate, $\vec{F}$ is a deterministic drift term encapsulating reaction and diffusion kinetics, and $\vec{\Xi}$ is a stochastic noise term. The force $\vec{F}$ is in general nonpotential, and the system is still high dimensional. To reduce this system to a more manageable form, we consider the limit of infinite reservoir diffusivity ($D_f \to \infty$), effectively treating the reservoir as a well-mixed, unstructured region where the concentrations $E_f^{\pm}$ are spatially uniform. Next, we assume that enzyme association and dissociation kinetics are much faster than molecular redistribution on the scaffold. On the characteristic timescale of phase separation, enzyme binding is thus effectively equilibrated, allowing for the adiabatic elimination of the enzyme degrees of freedom (see Appendix C). In this regime, the enzyme concentrations exhibit rapid stochastic variations, but their distribution is effectively slaved to the local substrate configuration, fluctuating around the local equilibrium:

$$K_d^{\pm} E^{\pm} = \phi^{\pm} E_f^{\pm}, \tag{4}$$

where $K_d^{\pm} = k_d^{\pm}/k_a^{\pm}$ (see Appendix C). On the other hand, the conservation of the total number of each enzyme species imposes a global constraint:

$$\gamma^{-1}\langle E^{\pm}\rangle_s + E_f^{\pm} = E_{tot}^{\pm}, \tag{5}$$

where $\langle \cdots \rangle_s$ denotes the spatial average over the scaffold, and γ is the ratio between the reservoir and scaffold geometric capacities (in the case of a three-dimensional cytosolic reservoir and a two-dimensional membrane scaffold, this would correspond to their respective volume-to-area ratio). Together, Eqs. (4) and (5) allow us to determine $E_f^{\pm}$ from $\langle \phi^{\pm}\rangle_s$.

It is finally convenient to change variables to the concentration difference ϕ and the total concentration c, defined as

$$\phi(\vec{x}, t) = \phi^+(\vec{x}, t) - \phi^-(\vec{x}, t), \tag{6a}$$

$$c(\vec{x}, t) = \phi^+(\vec{x}, t) + \phi^-(\vec{x}, t). \tag{6b}$$

Notably, the total concentration c is unaffected by interconversion reactions and purely diffusive; it thus exhibits random fluctuations around a homogeneous value determined by the initial conditions (see Appendix B). Neglecting the diffusive fluctuations in this homogeneous field (see Appendix B) allows the system dynamics to be reexpressed in terms of the single, locally nonconserved order parameter ϕ defined by Eq. (6a). This order parameter is subject to the constraint $-c \leqslant \phi \leqslant c$ and evolves according to the following stochastic equation, which, due to the nonanticipating nature of chemical reaction events, should be interpreted in the Itô sense (see Appendix B and Ref. [49]):

$$\partial_t \phi(\vec{x}, t) = D\Delta\phi(\vec{x}, t) + A[\phi] + \sqrt{B[\phi]}\,\xi(\vec{x}, t), \tag{7}$$

where $\xi(\vec{x}, t)$ is a zero-mean Gaussian white noise with

$$\langle \xi(\vec{x}, t)\xi(\vec{x}', t')\rangle = \delta(\vec{x} - \vec{x}')\delta(t - t'),$$

and the drift and noise terms are

$$A[\phi] = 2(R^+[\phi] - R^-[\phi]), \tag{8}$$

$$B[\phi] = 4(R^+[\phi] + R^-[\phi]), \tag{9}$$

with $\phi^{\mp} \to \phi^{\pm}$ conversion rates $R^{\pm}[\phi]$, incorporating both Michaelis-Menten enzymatic kinetics and basal first-order transitions, given by

$$R^{\pm}[\phi] = \frac{k_e^{\pm}[\phi]}{2} \frac{c^2 - \phi^2}{2\gamma K_m^{\pm} + c \mp \phi} + \frac{k_b^{\pm}}{2}(c \mp \phi) \tag{10}$$

and effective enzymatic rates $k_e^{\pm}[\phi]$ accounting for enzyme depletion via scaffold recruitment, with

$$k_e^{\pm}[\phi] = \frac{2k_c^{\pm}\gamma E_{tot}^{\pm}}{2\gamma K_d^{\pm} + c \pm \langle \phi\rangle_s}. \tag{11}$$

The multiplicative noise $\sqrt{B[\phi]}\,\xi(\vec{x}, t)$ in Eq. (7) is intrinsic, arising from the stochasticity of chemical reactions. Fast enzyme shuttling brings a correction of order $\epsilon = k_c/k_d$ to the noise amplitude $B[\phi]$ in Eq. (9) [see Appendix C for the complete expression, Eq. (C15)]. This correction is subdominant in the fast-exchange (adiabatic) regime, where the binding and unbinding of enzymes is much faster than catalysis, and is neglected here to maintain analytical tractability. The drift and noise terms [Eqs. (8) and (9)] are closely related, due to the Poissonian nature of the underlying chemical events.

The quadratic dependence on ϕ in the numerator of Eq. (10) is the signature of a local positive feedback. After adiabatic elimination of the enzyme degrees of freedom, this feedback arises from the underlying structure of the reaction

TABLE I. Concentration fields included in the model.

Symbols	Fields
$E_{\mathrm{f}}^{\pm}(t)$	Concentration of free $E^{\pm}$ enzymes in the unstructured reservoir
$E^{\pm}(\vec{x}, t)$	Concentration of $E^{\pm}$ enzymes on the scaffold
$\phi^{\pm}(\vec{x}, t)$	Concentration of $\phi^{\pm}$ molecules on the scaffold
$\phi(\vec{x}, t)$	Order parameter, representing the local composition difference: $\phi^{+}(\vec{x}, t) - \phi^{-}(\vec{x}, t)$
$\langle\phi(\cdot, t)\rangle_{\mathrm{s}}$	Spatial average of the field ϕ over the scaffold

network: enzymes are recruited to their own reaction products, generating an effective pairwise attraction between scaffold-bound molecules. It is worth noting here that nonlinearities emerging from both positive feedbacks and the Michaelis-Menten saturation mechanism can give rise to bistability [21,33,50].

The dependence of the effective enzymatic rates $k_{\mathrm{e}}^{\pm}[\phi]$ on the order parameter ϕ through its average $\langle\phi\rangle_{\mathrm{s}}$ in Eq. (11) encodes the effects of a global negative feedback: since the total enzyme count is finite, the sequestration of enzymes within domains enriched in one of the enzyme species depletes the available pool in the reservoir. This gives Eq. (7) the form of a time-dependent Ginzburg-Landau equation for a model A system [30] constrained by a global conservation law, which arises from the finite, shared pool of enzymes being rapidly exchanged across the system via the reservoir. The interplay between local self-reinforcement and global resource constraints constitutes the primary physical mechanism driving the appearance and stable coexistence of phase-separated domains [24–29].

A summary of the fields and parameters in the model is provided for convenience in Tables I and II.

The full dynamics of Eqs. (7)–(11) is still not analytically tractable. In the following, we exploit the fact that $\langle\phi\rangle_{\mathrm{s}}$ is a slow variable compared to the local field dynamics. We thus analyze the system adiabatically, treating $\langle\phi\rangle_{\mathrm{s}}$ as a fixed parameter, and later enforce the global constraint self-consistently for the determination of the steady states.

The stochastic dynamics of Eq. (7) can be formulated within the Martin-Siggia-Rose-Janssen–De Dominicis path-integral framework [51,52]. In this context, the stochastic evolution is mapped onto a path integral over the field ϕ and an auxiliary response field $\tilde{\phi}$ encoding noise realizations. This construction naturally introduces a generating functional, whose logarithm plays a role analogous to a free energy, as it generates correlation and response functions, while its extrema single out the most probable fluctuating trajectories [51,52]. This functional is explicitly constructed by averaging over noise distributed according to $P[\xi] \propto \exp(-\frac{1}{2}\int \mathrm{d}t \int \mathrm{d}\vec{x}\ \xi^2)$, while enforcing the Langevin equation as a constraint:

$$\int D\xi\ P[\xi] \int D\phi\ J[\phi]\ \delta(\partial_t\phi - D\nabla^2\phi - A - \sqrt{B}\,\xi),$$

where the Jacobian determinant J of the argument of the δ function is unity in the Itô regularization, which is the natural choice for intrinsic noise. Representing the δ function by means of the auxiliary response field $\tilde{\phi}$ and integrating out the noise, the generating functional can be recast as [52]

$$\int D\phi \int D\tilde{\phi}\ \mathrm{e}^{-S[\phi,\tilde{\phi}]},$$

with the action S and Hamiltonian H defined by

$$S[\phi, \tilde{\phi}] = \int \mathrm{d}t \int \mathrm{d}\vec{x} \left\{ \tilde{\phi}\,[\partial_t\phi - D\nabla^2\phi - A] - \frac{1}{2}B\tilde{\phi}^2 \right\}$$
$$= \int \mathrm{d}t \left\{ \int \mathrm{d}\vec{x}\ \tilde{\phi}\ \partial_t\phi - H[\phi, \tilde{\phi}] \right\}, \tag{12a}$$

$$H[\phi, \tilde{\phi}] = \int \mathrm{d}\vec{x} \left\{ \tilde{\phi}(A + D\nabla^2\phi) + \frac{1}{2}B\tilde{\phi}^2 \right\}. \tag{12b}$$

The most probable trajectories are the stationary points of S, which are determined by the Hamiltonian equations:

$$\partial_t\phi = \frac{\delta H}{\delta\tilde{\phi}} = A + D\nabla^2\phi + B\tilde{\phi}, \tag{13}$$

$$\partial_t\tilde{\phi} = -\frac{\delta H}{\delta\phi} = -\tilde{\phi}\frac{\delta A}{\delta\phi} - D\nabla^2\tilde{\phi} - \frac{1}{2}\tilde{\phi}^2\frac{\delta B}{\delta\phi}. \tag{14}$$

The steady-state solution $\tilde{\phi} = 0$ of Eq. (14) corresponds to deterministic relaxation, while solutions with $\tilde{\phi} \neq 0$ describe noise-activated trajectories.

III. MEAN-FIELD THEORY

Setting the response field $\tilde{\phi} = 0$ in Eqs. (13) and (14) yields the deterministic dynamics for the field ϕ in the form of a time-dependent Ginzburg-Landau equation:

$$\partial_t\phi(\vec{x}, t) = -\frac{\delta\mathcal{F}[\phi]}{\delta\phi(\vec{x}, t)}, \tag{15}$$

where the effective energy functional

$$\mathcal{F} = \int \left[\frac{D}{2}|\nabla\phi|^2 + V(\phi) \right] \mathrm{d}\vec{x} \tag{16}$$

with effective potential

$$V(\phi) = -\int A(\phi)\mathrm{d}\phi \tag{17}$$

plays a role analogous to that of the free energy in equilibrium systems. Here, the slowly varying spatial average $\langle\phi\rangle_{\mathrm{s}}$

TABLE II. Model parameters.

Symbols	Parameters
$k_{\mathrm{c}}^{\pm}$	Rate of $\mp \to \pm$ conversion
$K_{\mathrm{m}}^{\pm}$	Michaelis-Menten constant for $\mp \to \pm$ conversion
$k_{\mathrm{e}}^{\pm}$	Effective rate of $\mp \to \pm$ conversion, accounting for enzyme depletion from the reservoir
$k_{\mathrm{b}}^{\pm}$	Rate of $\mp \to \pm$ basal conversion
$k_{\mathrm{a}}^{\pm}$	Rate of $E^{\pm}$ binding to the scaffold
$k_{\mathrm{d}}^{\pm}$	Rate of $E^{\pm}$ unbinding from the scaffold
$K_{\mathrm{d}}^{\pm}$	Dissociation constant, defined as $k_{\mathrm{d}}^{\pm}/k_{\mathrm{a}}^{\pm}$
D	Macroscopic diffusivitiy on the scaffold
γ	Capacity ratio
c	Total concentration $\phi^{+} + \phi^{-}$
$E_{\mathrm{tot}}^{\pm}$	Total concentration of $E^{\pm}$ enzymes

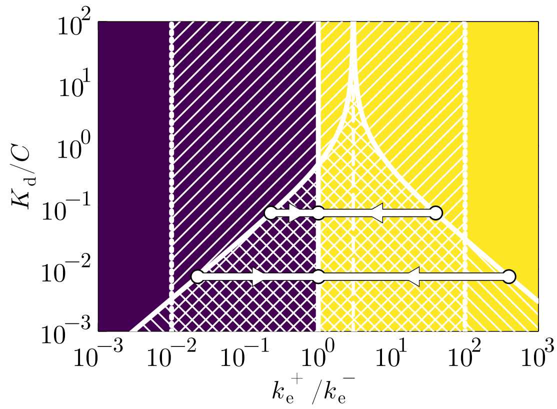

FIG. 2. Adiabatic relaxation of the catalytic ratio $\rho = k_e^+/k_e^-$ in the $(\rho, K_d/C)$ plane, for $K_m/C = 10^{-2}$, $\rho_0 = 3$, and $K_d^\pm = K_d$. The physically attainable states are restricted to the region between the solid boundary lines [Eq. (19)], which is centered at $\rho = \rho_0$ (dashed vertical line). Points on these boundaries represent uniform states, while the $\rho = 1$ solid vertical line corresponds to phase-coexistence steady states. The + and − phases are favored in the yellow ($\rho > 1$) and purple ($\rho < 1$) regions, respectively. The bistable region is enclosed by dotted lines [Eq. (18)]. The arrows illustrate the slow adiabatic drift as the system relaxes toward $\rho = 1$; the dependence of ρ on the order parameter $\langle\phi\rangle_s$ is governed by Eq. (11). For instance, a uniform state with $\langle\phi\rangle_s = -c$ corresponds to the right-hand boundary of the physical region (rightmost white dots). Here, random fluctuations trigger the growth of the competing + phase, which recruits corresponding enzymes from the reservoir. This depletion reduces ρ, thereby inducing an adiabatic drift toward the coexistence line (leftward arrows). Decay toward the phase-coexistence state occurs via homogeneous nucleation (upper leftward arrow) or linear instability (lower leftward arrow), depending on whether the initial uniform state lies within or outside the bistable region. An analogous behavior, mirrored across the $\rho = 1$ line, is observed for uniform states with $\langle\phi\rangle_s = +c$ (rightward arrows).

is treated as a fixed parameter, a condition we later relax by allowing it to vary adiabatically. To determine the mean-field phase diagram of the system, we study the behavior of the effective potential $V(\phi)$ as a function of kinetic rates and chemical concentrations. For simplicity, we set $K_m^\pm = K_m$ and neglect basal conversions since we focus on a regime where enzymatic processes dominate ($k_e \gg k_b$). The system exhibits a *bistability region* where the potential $V(\phi)$ has two minima, corresponding to stable phases $\phi = \pm c$, and a maximum at the unstable point $\phi_0 = (1 + 2\frac{K_m}{C})\frac{k_e^- - k_e^+}{k_e^+ + k_e^-}c$, where $C = c/\gamma$. This region (Fig. 2, hatched stripe) is defined by the following condition:

$$\frac{K_m}{K_m + C} \leqslant \frac{k_e^+}{k_e^-} \leqslant \frac{K_m + C}{K_m}. \tag{18}$$

The bistability region widens for smaller values of the Michaelis constant K_m, i.e., when enzymes operate close to the saturation regime. For $k_e^+ > k_e^-$, the unstable maximum is located at $\phi_0 < 0$, and the global minimum of the potential V is at $\phi = c$, favoring the + phase (Fig. 2, yellow stripe). Conversely, for $k_e^+ < k_e^-$, the unstable maximum is at $\phi_0 > 0$ and the global minimum is at $\phi = -c$, favoring the − phase (Fig. 2, purple stripe). When $k_e^+ = k_e^-$ the potential V is symmetric, the two phases are equally favored, and phase coexistence is possible at the steady state.

It is important to recall now that the $k_e^\pm$ rates are themselves slowly varying functions of the field configuration, through its spatial average $\langle\phi\rangle_s$. Therefore, not all ratios k_e^+/k_e^- are physically realizable, but only those compatible with the constraint $-c \leqslant \phi \leqslant c$. This defines the *physical region*:

$$\frac{\rho_0}{\rho_+} \leqslant \frac{k_e^+}{k_e^-} \leqslant \frac{\rho_0}{\rho_-}, \tag{19}$$

(Fig. 2, reverse hatched region) where

$$\rho_0 = \frac{k_c^+ E_{tot}^+}{k_c^- E_{tot}^-}, \quad \rho_+ = \frac{K_d^+ + C}{K_d^-}, \quad \rho_- = \frac{K_d^+}{K_d^- + C}. \tag{20}$$

A key implication is that the phase-coexistence steady state $k_e^+/k_e^- = 1$ is compatible with the physical constraint (19) only if the catalytic ratio ρ_0 satisfies

$$\rho_- \leqslant \rho_0 \leqslant \rho_+. \tag{21}$$

The above conditions allow us to derive the steady-state phase diagram of the system [Figs. 3(a) and 3(b)]. This diagram is defined in the reduced parameter space spanned by three dimensionless combinations of kinetic rates and molecular concentrations: $(\rho_0, K_d/C, K_m/C)$. The surfaces defined by $\rho_0 = \rho_\pm$ [solid lines in Figs. 3(a) and 3(b)] divide the parameter space in three regions, corresponding to steady states of either the pure + phase, the pure − phase, or a coexistence of both phases. The width of the phase-coexistence region is independent of the Michaelis constant K_m [Fig. 3(b)] but widens for smaller dissociation constants K_d [Fig. 3(a)], i.e., when enzymes from the reservoir have higher affinity for the scaffold.

The phase-coexistence region in its turn is divided in two subregions, corresponding to distinct pathways of relaxation toward the steady state. Starting from one of the uniform initial states that are at the extremes of the physical region, $\langle\phi\rangle_s = \pm c$, the system can exhibit two qualitatively different relaxation mechanisms. If the initial uniform state is within the bistability region, it is metastable (as illustrated in Fig. 2, and detailed in its caption) and decays via nucleation of droplets of the globally favored phase [Fig. 3(c)]. Conversely, if the initial uniform state is outside the bistability region, it is linearly unstable, and phase separation is triggered spontaneously by small fluctuations. The metastable and unstable regions are separated by the surfaces [Figs. 3(a) and 3(b), dashed lines]:

$$\rho_0 = \frac{K_m + C}{K_m}\rho_-, \quad \rho_0 = \frac{K_m}{K_m + C}\rho_+. \tag{22}$$

A global negative feedback mechanism governs the long-term dynamics. The favored phase is determined by the ratio $\rho = k_e^+/k_e^-$, which, according to Eq. (11), is a decreasing function of the spatial average $\langle\phi\rangle_s$ of the order parameter. This establishes a self-regulating loop: as the growth of + phase domains increases $\langle\phi\rangle_s$, it simultaneously drives the ratio ρ downward. This process induces the adiabatic drift illustrated in Fig. 2 (white leftward arrows), pushing the system asymptotically toward phase coexistence, where $\rho = 1$

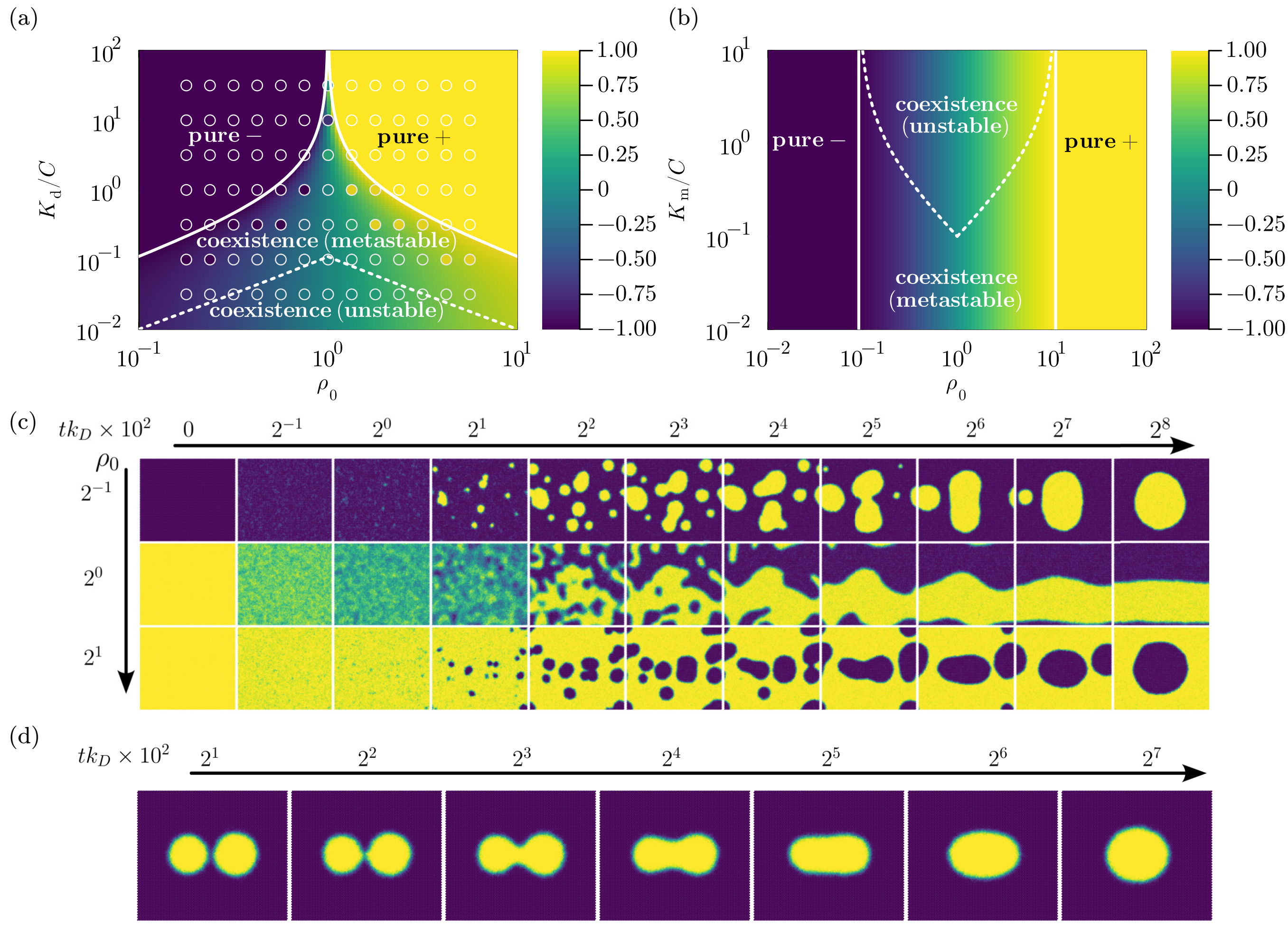

FIG. 3. Steady-state phase diagram in the reduced parameter space (ρ_0, K_d/C, K_m/C): (a) a projection on the (ρ_0, K_d/C) plane with K_m/C fixed at 0.1 and (b) a projection on the (ρ_0, K_m/C) plane with K_d/C fixed at 0.1. We consider here $K_\mathrm{d}^+ = K_\mathrm{d}^- = K_\mathrm{d}$ and $K_\mathrm{m}^+ = K_\mathrm{m}^- = K_\mathrm{m}$. The solid white lines, defined implicitly by the conditions $\rho_0 = \rho_\pm$ [Eqs. (20) and (21)] from the mean-field theory, separate regions of pure phases from regions of phase coexistence. The dashed white lines distinguish metastable from unstable regions. The background color represents the theoretical prediction for the steady-state order parameter $\langle\phi\rangle_{\mathrm{s},\infty}/c$ from Eq. (23). The color inside each circle denotes the measured $\langle\phi\rangle_\mathrm{s}/c$ in the final time $t = 10^5 k_D^{-1}$ of a numerical simulation with the corresponding parameters. (c) Time evolution of field configurations from simulations with different ρ_0 values, tuned via the ratio $E_\mathrm{tot}^+/E_\mathrm{tot}^-$. Here, $K_\mathrm{d}/C = 0.1$. The mechanism of phase separation depends on ρ_0, and can proceed via either nucleation or linear instability, as predicted in panels (a) and (b). The color scale is the same as in the phase diagram above. Simulations are performed with $k_\mathrm{b} \sim 10^{-3} k_\mathrm{e}^{\max}$ (see Appendix G). (d) Domain coalescence driven by interface minimization. The simulation shows the merging of two initially separate domains, driven by minimization of the effective energy $\mathcal{F}$ concentrated at phase interfaces.

and catalytic actions are balanced. Physically, the expansion of a stable phase depletes the reservoir of available enzymes of the corresponding type, recruiting them from the cytosol and slowing further growth until the system relaxes into a phase-coexistence steady state. Here, the spatial average of the field reaches a value

$$\langle\phi\rangle_{\mathrm{s},\infty} = \frac{\left(1 + 2\frac{K_\mathrm{d}^-}{C}\right)\rho_0 - \left(1 + 2\frac{K_\mathrm{d}^+}{C}\right)}{\rho_0 + 1}\, c, \tag{23}$$

which determines the fraction of the scaffold occupied by each phase (see Appendix D). During relaxation to this steady-state asymptotics the variation of $\langle\phi\rangle_\mathrm{s}$ becomes slower and slower, which justifies *a posteriori* the adiabatic assumption. A similar argument validates the adiabatic assumption during the nucleation of small domains of the stable phase within a metastable background.

We tested these mean-field predictions with numerical simulations of the full stochastic process [Eqs. (1)–(3)] on a discrete lattice using the Gillespie algorithm (see Appendix G for simulation details and parameters). Our numerical exploration of the phase diagram shows good qualitative agreement with the mean-field prediction [Figs. 3(a) and 4]. However, a quantitative mismatch occurs near the phase boundaries. This discrepancy arises because the escape time from metastable uniform states diverges near these boundaries (see Sec. IV). Since simulations are run for a finite time, configurations near the predicted boundaries (corresponding to some of the symbols near $\pm c$ in Fig. 4) do not reach the true steady state over the simulation time. In contrast, simulations deep

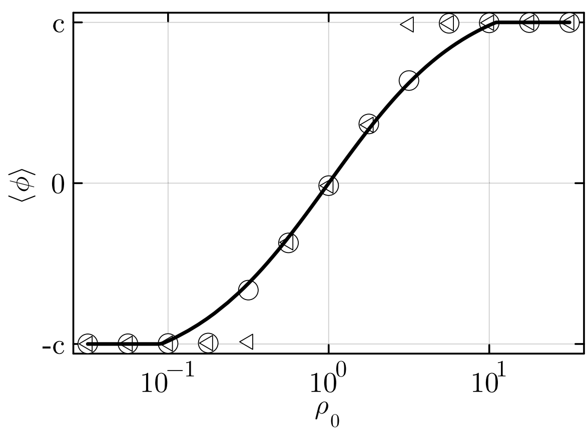

FIG. 4. Numerical measurements (symbols) of the steady-state average $\langle\phi\rangle_s$ compared with the theoretical prediction (solid line). The parameter ρ_0 is varied by independently tuning either the catalytic rates $k_c^\pm$ (circles) or the total enzyme concentrations $E_{tot}^\pm$ (diamonds). Simulations are performed with $K_d/C = 0.1$ and $K_m/C = 0.1$.

within the phase-coexistence region agree very well with the theory. The data in Fig. 4, obtained by separately varying the catalytic rate k_c^+ and the total enzyme number E_{tot}^+, confirm that phase coexistence is controlled by their product within the dimensionless ratio ρ_0 [Eq. (20)]. It is worth noting here that for larger dissociation rates K_d, fewer enzymes are bound to the scaffold, the effective catalytic rates $k_e^\pm$ decrease, and the time required to reach the steady state in the simulations increases accordingly.

This theoretical scenario qualitatively reproduces experimental observations in a reconstituted kinase-phosphatase system [21]. There, a pair of antagonistic enzymes, a lipid kinase and a phosphatase, catalyze the interconversion between the lipid states PI(4)P and PI(4,5)P_2 on a membrane surface. The kinase exhibits a positive feedback by preferentially binding to its product, thereby recruiting more kinase to the membrane, and the phosphatase is genetically engineered to implement an analogous feedback mechanism. Our theoretical phase diagram is compatible with their experimental observations, in particular with the time-lapse data obtained by varying enzyme concentrations (see Fig. 5). Notably, the active character of the phase-ordering process is confirmed by their experimental observation that domains disappear upon ATP removal (see Fig. S8 from Ref. [21]).

Furthermore, our theoretical framework is consistent with observations of Rab5 domain formation on synthetic membranes [23]. In this system, which plays a crucial role in endocytic protein sorting, the small GTPase Rab5 acts as a two-state molecule, switching between inactive (GDP-bound) and active (GTP-bound) states. The Rabex5/Rabaptin5 complex functions as the catalytic unit that binds the active state (GTP-Rab5) and promotes the transition from the inactive to the active state, thus creating a positive feedback loop. By varying the concentration of the catalytic unit, they observe a transition from a homogeneous state to one with stable domains (see Figs. 3(B)–3(D) from Ref. [23]), which closely

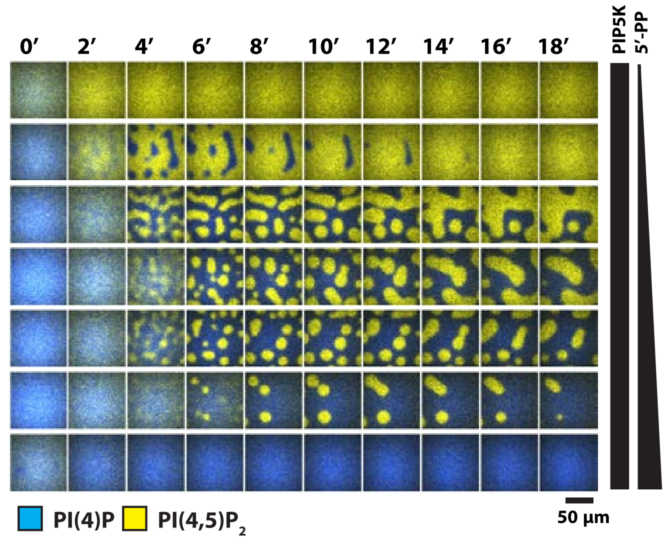

FIG. 5. Time evolution of lipid domains in an *in vitro* reconstituted kinase-phosphatase reactions system. Two antagonistic enzymes, the PIP5K kinase and INPP5E phosphatase, drive the interconversion of the membrane lipids PIP(4,5)P and PI(4)P; these correspond to E^+, E^-, ϕ^+, and ϕ^- in our model, respectively. Rows from top to bottom correspond to increasing concentrations of INPP5E (5’-PP gradient bar) at a fixed concentration of PIP5K, thereby varying the enzyme concentration ratio. Starting from the same initial conditions, the onset of phase separation and a subsequent coarsening process are observed over time for a range of these ratios. Consistent with our theoretical prediction [Eq. (20)] and numerical results [see Figs. 3(a) and 3(c)], this ratio controls the membrane fraction occupied by each phase. This figure is reproduced from Ref. [21].

mirrors the phase transition predicted by our theoretical phase diagram.

The dynamics of sufficiently large phase-separated domains is nearly deterministic and governed by Eq. (15), which shows that the system evolves to minimize the effective energy in Eq. (16). At large times, this leads to relaxation to the stationary state:

$$0 = \frac{\delta\mathcal{F}[\phi]}{\delta\phi(\vec{x},t)} = -D\nabla^2\phi(\vec{x},t) + V'(\phi(\vec{x},t)). \tag{24}$$

For a flat interface at coexistence (where the potential is symmetric, $\phi_0 = 0$, and $V(\pm c) = 0$) separating regions occupied by the $-c$ and $+c$ phases, this equation is readily integrated along a coordinate x transverse to the interface to give $\frac{D}{2}(\partial_x\phi)^2 = V(\phi)$. Approximating $V(\phi)$ with a fourth-order polynomial (see Appendix E), this equation can be solved explicitly to obtain the interface profile $\phi(x) = c\tanh(x/w)$, exhibiting the width

$$w = \frac{4Dc^2}{3\sigma}, \tag{25}$$

where σ is an effective interfacial tension (effective energy per unit interface length or area, depending on whether the scaffold is two or three dimensional), expressed in terms of nonequilibrium kinetic rates:

$$\sigma = \int_{-\infty}^{+\infty} \left[\frac{D}{2}(\partial_x\phi)^2 + V(\phi)\right]\mathrm{d}x \tag{26}$$

$$= D\int_{-\infty}^{+\infty} (\partial_x\phi)^2\,\mathrm{d}x \tag{27}$$

$$= \int_{-c}^{+c} \sqrt{2DV(\phi)}\,\mathrm{d}\phi \tag{28}$$

$$= \frac{4}{3}\sqrt{D(k_e^+ + k_e^-)g(K_m/C)}\,c^2, \tag{29}$$

and

$$g(\kappa) = 1 + 4\kappa(1+\kappa)\ln\frac{4\kappa(1+\kappa)}{(1+2\kappa)^2} \tag{30}$$

is a monotonically decreasing function with $g(0) = 1$ and $g(\kappa) \sim \kappa^{-2}$ for large κ. Therefore, the interfacial tension is larger when enzymes operate near their saturation regime (smaller K_m). This decrease of σ with large K_m is a genuine consequence of saturation-induced nonlinearity, as it persists even when the limit is taken at constant $k_\mathrm{e}^\pm/K_\mathrm{m}$ to normalize for the reduced reaction rate [Eq. (11)].

Together, Eqs. (25) and (29) show that enzymes working near saturation and/or with faster catalytic rates produce sharper interfaces. This can be intuitively understood as follows: self-reinforcing catalytic conversions induce effective interactions between scaffold-bound molecules. More frequent catalytic conversions, driven by either larger $k_\mathrm{c}^\pm$, smaller K_m, or both, induce stronger effective interactions and result in higher interfacial tension and sharper interfaces. Importantly, these effective interactions are purely kinetic and do not require sustained molecular proximity. In this context, the high interfacial tension is a macroscopic manifestation of the rate at which the system dissipates energy to maintain the compositional gradient against diffusive mixing.

The interfacial width can be used to experimentally measure the interfacial tension via Eq. (25), provided the other parameters are known. Our direct numerical measurements of w confirm its predicted dependence on the key catalytic parameters, $k_\mathrm{e}^\pm$ and K_m (Fig. 6).

Sharp boundaries and high interfacial tension are typically associated with strong, site-specific molecular interactions [5]. Our active scenario, which is founded on intrinsically site-specific enyzmatic interactions, demonstrates that interface sharpness is governed not merely by binding strength but also decisively by the frequency of catalytic events.

Since the effective energy $\mathcal{F}$ from Eq. (16) is concentrated at phase interfaces, the dynamics of large domains is driven by the minimization of the total interface length. This leads to the coalescence of nearby domains into larger ones to reduce the interface length, as illustrated in simulations where two initially separate domains merge [Fig. 3(d)].

Overall, these results show that a gas of reacting and diffusing particles can exhibit at the mesoscopic scale a phenomenology nearly indistinguishable from that of classical phase separation. This process includes domain formation via nucleation or linear instability, and coarsening driven by interface minimization [Figs. 3(c) and 3(d)]. However, two key

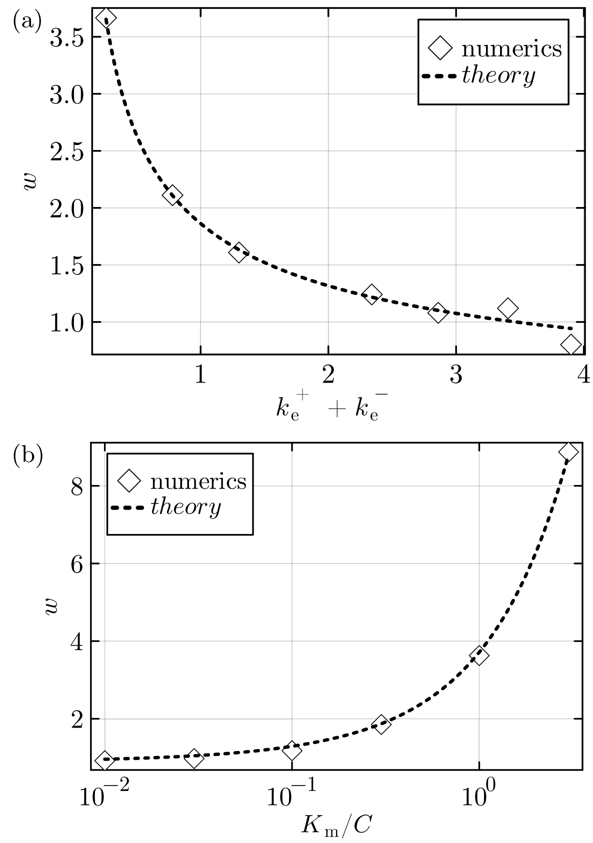

FIG. 6. Numerically determined interface width w (in lattice units) for circular domains at the steady state. (a) Interface width as a function of the total catalytic rate $k_\mathrm{e}^+ + k_\mathrm{e}^-$. (b) Interface width as a function of the Michaelis constant K_m. Solid curves are fits to Eq. (25), with the prefactor as a free parameter. Error bars are smaller than the plot markers. The interface width is determined by computing the radial average of the field around a stationary domain and fitting the resulting profile to a hyperbolic tangent. Parameters are listed in Table III.

distinguishing features, which could be used for experimental discrimination, must be emphasized.

First, since the particles behave as a gas, particle exchange across boundaries is rapid. The stability of domains does not arise from reduced particle mobility, but from their constant interconversion, driven by enzymatic activity at the interfaces (see Fig. 7, right-hand inset).

Second, as a direct consequence, maintaining the domain structure requires a constant energy expenditure. The power consumption per unit interface length associated with the interfacial activity of each enzyme type can be computed by integrating the reaction rates (10) over the previously derived flat interface profile, obtaining

$$\mathcal{P}^\pm = \frac{1}{2}k_\mathrm{e}^\pm \varepsilon_0 c w \ln\left(1 + \frac{C}{K_\mathrm{m}}\right), \tag{31}$$

where ε_0 is the energy expended in a single catalytic event, which is typically provided by the hydrolysis of a single ATP molecule [1]. Equation (31) shows that the power required to maintain a phase interface is proportional to the width of the interface and is thus inversely proportional to the interface

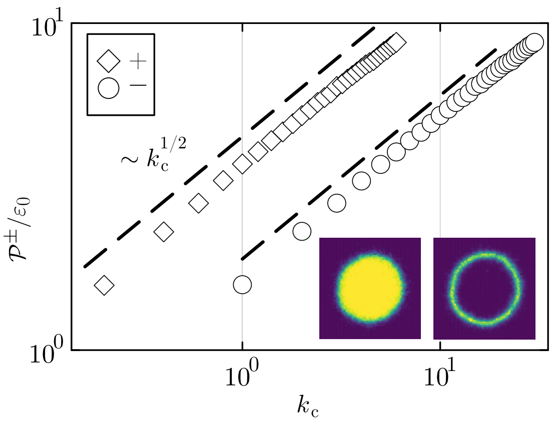

FIG. 7. Power consumption per unit interface length as a function of the catalytic rate k_c for both enzyme species (diamonds, +; circles, −). Numerical measurements of the frequency of catalytic events are compared with the predicted $\sim k_c^{1/2}$ scaling (dashed lines). Left inset: A system configuration showing a domain of the + phase (yellow) within the − phase (purple). Right inset: The corresponding spatial distribution of power consumption, where yellow indicates the maximum value and purple indicates zero. Energy dissipation is concentrated at the phase interface, where futile cycles of antagonist reactions take place.

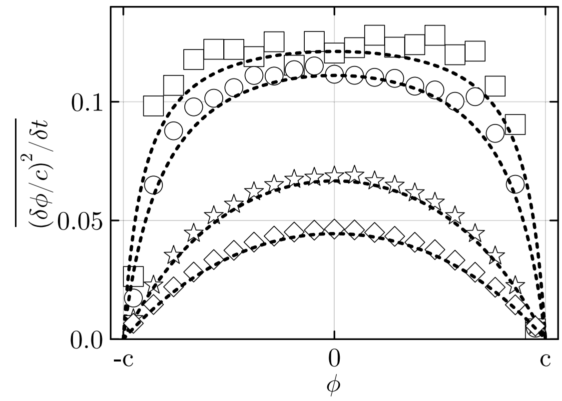

FIG. 8. Amplitude of field fluctuations as a function of the local field value ϕ. Symbols show binned numerical data for different Michaelis constants K_m/C: 0.05 (squares), 0.1 (circles), 0.5 (stars), and 1 (diamonds). Simulations were performed with $k_b^{\pm} = 0$ and a symmetric potential, resulting in a fluctuation peak at $\phi = 0$. Solid lines correspond to the theoretical model [Eq. (9)]. Error bars are smaller than the symbol sizes.

tension. Combining Eqs. (25) and (29)–(31) shows that the power consumption is a slowly decreasing function of K_m, with a logarithmic divergence for $K_m \ll C$ stemming from the breakdown of the Michaelis-Menten approximation. From the same relations we find that the power consumption scales with the square root of the catalytic rates $k_c^{\pm}$, a scaling confirmed by numerical measurements (Fig. 7).

IV. FLUCTUATIONS

The decay of a uniform state into a spatially patterned state is a crucial process in biological membranes, underlying phenomena such as chemotaxis [53,54], asymmetric cell division [55,56], proliferation [57,58], immune signaling [59], and protein sorting [60–62]. Linearly unstable uniform states tend to decay immediately and are thus unlikely to be directly observable in real time. In contrast, metastable uniform states can persist for long periods before decaying into a polarized, phase-separated state, either spontaneously via homogeneous nucleation or triggered by a small external cue [63]. Fluctuations, not considered in previous sections, are crucial for nucleation. In our simulations, we observe that germs of the stable phase of size smaller than a critical size R_c tend to shrink, while those larger than R_c grow into stable domains, mirroring the phenomenology of equilibrium phase separation. In this nonequilibrium setting, the properties of nucleation and the dependence of the critical size on the kinetic parameters of the process can be investigated using large-deviation theory [64–66]. This approach must account for the multiplicative nature of the noise [Eqs. (9)–(11)], which itself depends on the field configuration ϕ. Figure 8 compares the analytical prediction for the noise amplitude $B(\phi)$ [Eq. (9)] with direct simulation measurements. Consistent with the theoretical limit assumed in the derivation (Appendix C), the simulations are performed in the regime of negligible enzyme fluctuations (cf. Table III), showing good agreement.

When basal catalysis is switched off ($k_b = 0$), the noise amplitude vanishes in the uniform states $\phi = \pm c$, making them absorbing: configurations from which the system cannot escape spontaneously. This is reminiscent of the absorbing consensus states in generalized voter models [67–71]. In this analogy, the $\phi^{\pm}$ molecules can be seen as voters in two opinion states, and the catalytic enzymes as agents that facilitate opinion changes.

Figure 8 also shows that, according to Eq. (9), noise near uniform states is less suppressed for smaller K_m (i.e., when enzymes operate near saturation). Due to the Poissonian character of reaction events, both the amplitude of field fluctuations and the local energy dissipation are proportional to the overall reaction rate [Eq. (9)]. Consequently, $B(\phi)$ is minimal in the bulk of phase-separated domains ($\phi \sim \pm c$) and maximal at the intermediate ϕ values characteristic of phase interfaces (Fig. 8 and right-hand inset of Fig. 7).

The nucleation probability P for a critical germ is controlled by a large-deviation rate function $S \sim -\log P$, which depends on the noise amplitude $B(\phi)$. The most probable trajectory out of a metastable uniform state is the "activated" trajectory, i.e., the optimal fluctuation that effectively reverses the deterministic relaxation dynamics, allowing the system to climb the free-energy barrier. In our case, the trajectory connecting the uniform state to a circular domain of radius R is given by the solution of Eqs. (13) and (14), evaluated along the activated trajectory. Along this path, the auxiliary field satisfies $\tilde{\phi} = -2\frac{A+D\nabla^2\phi}{B}$ [52], yielding

$$S[\phi] = \int \mathrm{d}\vec{x} \int \mathrm{d}t \left\{ -2\frac{A[\phi] + D\nabla^2\phi}{B[\phi]} \partial_t \phi \right\}. \qquad (32)$$

We look for the extremal trajectory in the form of a growing circular droplet, $\phi(\vec{x}, t) = \phi(r - R(t))$, allowing S to be reparametrized as a function of the droplet radius R. For a small critical germ, the dependence of $\langle\phi\rangle_s$ on R is negligible. We thus treat $\langle\phi\rangle_s$ as a constant, reducing the functionals

TABLE III. Simulation parameters. An asterisk (∗) denotes parameters that are varied in the corresponding plot. Lengths are expressed in units of $\Omega^{1/2}$, the timescale is set by $k_D = 10^{-1}$, $n_{\rm tot}/L^2 = 10^2$, and $k_{\rm e}^{\max} = \max\{k_{\rm e}^+, k_{\rm e}^-\}$.

Figure	$k_{\rm c}^+$	$k_{\rm c}^-$	$k_{\rm d}^\pm$	$k_{\rm a}^\pm$	$\gamma K_{\rm m}^+$	$\gamma K_{\rm m}^-$	$\frac{k_{\rm b}^\pm}{k_{\rm e}^{\max}}$	$\frac{n_{\rm tot}^{E\pm}}{L^2}$	Initial configuration
3(a)	∗	∗	∗	10	1	1	10^{-2}	1	Random 50% mixture
3(c)	∗	∗	10	10	1	1	10^{-2}	1	Uniform state
3(d)	1	0.27	5	5	5	10	0	1	Two domains of + phase
4	∗	∗	20	20	10	10	10^{-3}	∗	Random 50% mixture
6(a)	∗	∗	10	10	10	10	0	1	Single domain of + phase
6(b)	1	5	10	10	∗	∗	0	1	Single domain of + phase
8	10	10	100	100	∗	∗	0	20	Random 50% mixture
9(a), 9(b)	1	1	∗	10	10	10	0	1	Single domain of + phase
9(c)	1	1	∗	10	10	10	10^{-3}	1	Uniform pure − state

$A[\phi]$, $B[\phi]$ to local functions $A(\phi)$, $B(\phi)$ and their functional derivatives to ordinary ones. In the limit of negligible interface width ("thin-wall approximation") and negligible basal catalysis, the maximum of S is found at the critical value (cf. Appendix F)

$$R_{\rm c} = -\frac{\int_{-c}^{c} \frac{\phi'}{B(\phi)} \mathrm{d}\phi}{\int_{-c}^{c} \left\{\frac{2}{D}\frac{A(\phi)}{B(\phi)} + \frac{\phi'^2 B'(\phi)}{[B(\phi)]^2}\right\} \mathrm{d}\phi}. \tag{33}$$

Note that Eq. (32) describes only the noise-driven, activated path to the critical droplet, since the subsequent growth follows a deterministic path. Using a polynomial approximation for the potential and noise terms, we obtain an explicit expression for the critical radius:

$$R_{\rm c} = \frac{3}{20} f(K_{\rm m}/C) \frac{\sqrt{D(k_{\rm e}^+ + k_{\rm e}^-)}}{|k_{\rm e}^+ - k_{\rm e}^-|}, \tag{34}$$

where

$$f(\kappa) = \frac{1 + 2\kappa}{\left[1 + \frac{12}{5}(\kappa + \kappa^2)\right]\sqrt{g(\kappa)}} \tag{35}$$

is a monotonically increasing function with $f(0) = 1$ (see Appendix F). The critical radius is thus smaller for enzymes operating near saturation (smaller $K_{\rm m}$) and for a larger kinetic asymmetry between the two competing enzymatic reactions (larger $|k_{\rm e}^+ - k_{\rm e}^-|$). It also depends on kinetic rates through $k_{\rm e}^\pm$. Equations (11) and (34) show that $R_{\rm c}$ is smaller for smaller $K_{\rm d}$, i.e., for stronger enzyme affinity for the scaffold. The nonequilibrium nature of the present result is manifested in its dependence on kinetic parameters. In addition, the peculiar numerical prefactor stems from a distinct contribution proportional to $B'(\phi)$ that would be absent if noise were purely additive. Finally, the nucleation radius depends on the average composition $\langle\phi\rangle_{\rm s}$ through the effective catalytic rate $k_{\rm e}$, reflecting the constraints imposed by the global conservation law.

To numerically estimate $R_{\rm c}$ in the full stochastic process [Eqs. (1)–(3)], we initialize circular domains of various sizes and monitor their evolution. Smaller domains shrink and disappear, while larger ones grow to a stationary state. The critical radius is identified as the size for which 50% of domains survive [19,72] [see Fig. 9(a)].

The analytic expression for the critical radius, Eq. (34), is derived using several idealizations needed for tractability: the continuum Langevin description, circular droplet ansatz, thin-wall approximation, nearly symmetric effective potential, and the omission of subdominant enzyme noise. Despite these simplifications, direct numerical simulations of nucleation from a uniform metastable phase confirm the predicted functional dependence of the critical radius $R_{\rm c}$ on the dissociation constant $K_{\rm d}$, up to an order-one fitting factor [Fig. 9(b)], that could also be related to the contribution of nontrivial out-of-equilibrium droplet shape fluctuations [73].

Larger critical sizes are expected to correspond to lower nucleation rates for the stable phase within the metastable uniform state. This is confirmed by simulation results where, with a low level of basal catalysis ($k_{\rm b}^\pm = 10^{-3} k_{\rm e}^{\max}$) maintained to avoid the absorbing state, we find that, for increasing $K_{\rm d}$ (and thus increasing critical radius), the system lingers in the metastable state for progressively longer and more variable times before a critical germ nucleates and grows almost deterministically to the steady state [Fig. 9(c)].

V. CONCLUSIONS

Active phase separation is emerging as a key physical paradigm for intracellular organization, driven by nonequilibrium processes where energy consumption governs the formation of spatial patterns [6,7,9,13,18,29]. This framework offers a unifying perspective on biological phenomena, including the assembly of polarized signaling patches on membranes, that have often been described in the past through the lens of "pattern formation." Indeed, these processes may exhibit the canonical phenomenology of equilibrium phase separation, including domain coalescence, coarsening, and phase ordering driven by interfacial tension, yet they operate through fundamentally different physical mechanisms.

Here, we formalize a minimal model of an enzyme-driven phase-ordering process, grounded in a well-defined biological module: the counteracting enzymes that govern the activation state of membrane-bound signaling proteins. Our formulation incorporates two realistic ingredients, local reinforcing feedback loops and global constraints imposed by rapid exchange with an enzymatic reservoir, while still remaining analytically tractable. This structure places the model in the class of locally nonconserved (model A) dynamics with a global constraint on the total fraction of each molecular state, which is a fundamental mechanism enabling phase coexistence

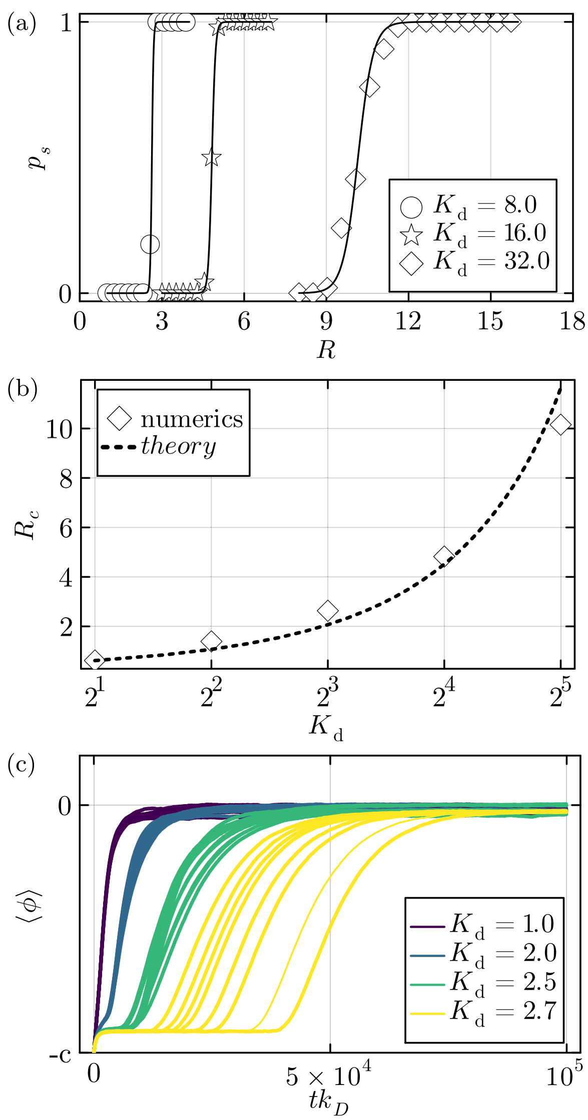

FIG. 9. Nucleation dynamics and critical radius. (a) Survival probability p_s of an initial domain as a function of its radius R (in lattice units) for different values of K_d. The critical radius R_c for each curve is estimated as the radius where $p_s = 1/2$. (b) The critical radius R_c as a function of the dissociation constant K_d. The dotted line is a fit of the theoretical prediction from Eq. (34), with $k_e^{\pm}$ from Eq. (11); a global scaling factor of approximately 3 was applied to the theoretical curve to achieve a best fit with the numerical data. (c) Time evolution of the field average $\langle\phi\rangle_s$ from simulations starting in a homogeneous state. For smaller K_d (purple, blue), the state is linearly unstable and separates immediately. For larger K_d (green, yellow), the state is metastable, exhibiting a stochastic escape time before separation. Each color represents multiple trajectories. All simulations have balanced activity ($\rho_0 = 1$, yielding $\langle\phi\rangle_{s,\infty} = 0$) and include a low basal catalysis rate $k_b^{\pm} = 10^{-3}k_e^{\max}$ to avoid absorbing states. The initial small ramp is due to the slight shift in the minimum of the potential when $k_b^{\pm} > 0$. For increasing K_d, the system lingers in the metastable, homogeneous $-$ state for longer and more variable times until a critical germ of the $+$ phase nucleates and grows deterministically to the steady state.

[24–29]. Mean-field theory yields an explicit phase diagram and closed-form expressions for key observables, including interfacial tension and phase-coexistence boundaries, in terms of basic kinetic rates. The model's simplicity further allows us to move beyond mean-field approximations and analytically investigate fluctuation-driven events. Using large-deviation theory, we derive an explicit expression for the critical nucleation radius, which quantifies the stochastic transition from a metastable uniform state to a phase-separated one via the formation of critical droplets. The quantitative accuracy of our analytical approaches, from mean-field to nucleation theory, is validated through extensive stochastic simulations of the underlying particle-level model, confirming that the simplified theory captures the essential physics of the full system.

In equilibrium phase separation, the onset of phase ordering is controlled by equilibrium parameters such as saturation concentrations. Here, an analogous role is played by intrinsically nonequilibrium parameters, such as kinetic rates and enzyme concentrations. The system exhibits abrupt changes in its properties when specific, dimensionless combinations of these parameters exceed a critical threshold, a direct analog of equilibrium criticality. Thus, the hallmark feature of a robust threshold response, a well-established mechanism for cellular switches between qualitatively different behaviors [74,75], can be preserved and implemented here through intrinsically nonequilibrium means.

Our analysis yields explicit conditions for phase coexistence, showing it is promoted by a higher enzyme affinity for the membrane and by asymmetries in both enzyme numbers and catalytic activities. Furthermore, we demonstrate that the metastability of uniform states and the sharpness of interdomain interfaces are enhanced when enzymes operate near saturation. Critically, phase ordering is driven here by energy-consuming, nonequilibrium processes. Unlike equilibrium phase separation, the establishment and maintenance of interfaces require continuous energy expenditure. This dissipation is minimal within the bulk of the domains and maximal at the interfaces, where incessant enzymatic "futile" cycles sustain the phase separation. Our theory provides closed-form expressions for directly observable quantities, such as interface width, domain area fraction, and critical nucleation radii, offering a set of testable predictions that are directly accessible to targeted experiments.

While the system described here shares much of the phenomenology of equilibrium phase separation, including an effective dynamics that minimizes an effective interfacial energy, its underlying physics is distinct. The interactions driving the ordering process do not require continuous direct contact, but are mediated by pointlike, intermittent enzymatic events. This permits the formation of ordered, persistent structures even from a dilute, gaslike phase. In such a scenario, rapid exchange of material between domains and the surrounding environment is expected to be the rule. This rapid exchange, frequently observed in fluorescence recovery after photobleaching (FRAP) experiments [3,21,23,76] and often attributed to the liquid character of condensates, would be even more pronounced for gaslike domains, such as the persistent membrane-associated domains observed in chemotaxing cells [77].

A central challenge in applying equilibrium phase separation to biomolecular condensates lies in its frequent reliance on nonspecific molecular interactions, which can seem at odds with the highly regulated, combinatorial logic of cellular biochemistry [5]. Enzyme-driven phase separation, being intrinsically based on site-specific enzymatic activity, is a universal mechanism that intrinsically supports the regulated, combinatorial character inherent to cell physiology. While we consider here the simplest module consisting of a couple of counteracting enzymes and their membrane-bound substrates, it is quite easy to imagine numerous such modules, involving diverse enzymatic feedback loops, operating in parallel and interacting in various ways (a few illustrative examples are given in Appendix H).

Qualitatively, the presented scenario of active phase separation aligns with experimental observations of reconstituted membranes. The agreement spans distinct biochemical systems, capturing the evolution of lipid domains governed by a kinase-phosphatase pair [21] as well as the formation of protein domains driven by a GTPase and its GEF-effector complex [23]. The experimentally demonstrated dissolution of domains upon ATP removal [21] underscores in those systems the essential role of energy consumption, which is a cornerstone of our theoretical framework. The ability of our minimal model to describe such biochemically disparate systems suggests that its underlying principles, grounded in nonequilibrium thermodynamics and stochastic kinetics, constitute a general physical mechanism for domain formation on molecular scaffolds, including cell membranes as a primary example.

ACKNOWLEDGMENTS

We gratefully acknowledge fruitful discussions with Guido Serini, Carlo Campa, and Andrea Musacchio. Numerical calculations were performed using resources of the Leonardo cluster at CINECA under a CINECA-INFN agreement.

DATA AVAILABILITY

The data that support the findings of this article are openly available [78].

APPENDIX A: MICROSCOPIC MODEL

The system, defined by the chemical reactions in Eqs. (1)–(3), together with molecular diffusion, is discretized on an $L \times L$ hexagonal lattice with periodic boundary conditions, representing a lipid membrane scaffold exchanging particles with an unstructured reservoir. The system state at any instant of time is given by the number of molecules $n_i^+, n_i^-, n_i^{E^+}, n_i^{E^-}$ at each site $i = 1, \dots, L^2$ and the numbers $n_\mathrm{f}^{E^+}, n_\mathrm{f}^{E^-}$ of free enzymes in the reservoir (see Fig. 10). The following independent Poisson processes are considered:

(1) A molecule diffuses to a neighboring cell with rate $k_D n_i^{\pm}$.

(2) An enzyme diffuses to a neighboring cell with rate $k_D n_i^{E^\pm}$.

(3) One $\mp$ molecule is converted via enzymatic catalysis to one $\pm$ molecule, mediated by enzymes $E^{\pm}$ at a site, with rate $\frac{k_\mathrm{c}^{\pm} n_i^{E^\pm} n_i^{\mp}}{\gamma \Omega K_\mathrm{m} + n_i^{\mp}}$, where K_m is a Michaelis constant.

(4) A $\mp$ molecule is converted to a $\pm$ molecule with rate $k_\mathrm{b}^{\pm} n_{\mp}^{i}$.

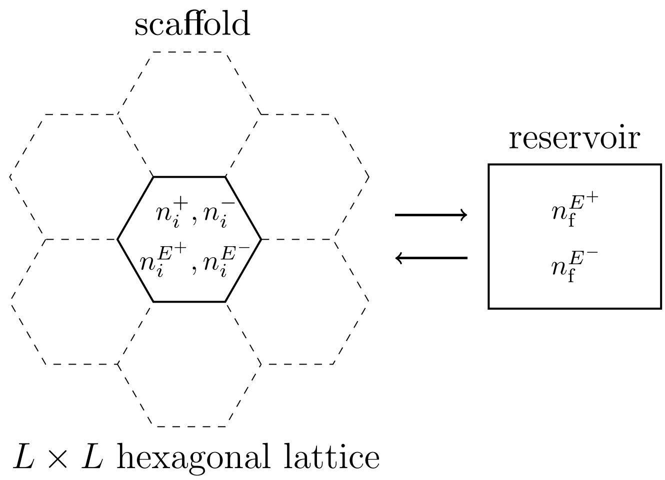

FIG. 10. Schematic of the discrete system implemented in the simulations. The scaffold is modeled as an $L \times L$ hexagonal lattice; within each cell i, $n_i^{\pm}$ and $n_i^{E^\pm}$ denote the number of $\phi^{\pm}$ molecules and bound $E^{\pm}$ enzymes, respectively. The unstructured reservoir contains $n_\mathrm{f}^{E^\pm}$ free enzymes.

(5) A free enzyme $E_\mathrm{f}^{\pm}$ from the reservoir is attached to a site i, promoted by the presence of its product molecule ($\pm$), with rate $k_\mathrm{a}^{\pm} n_\mathrm{f}^{E^\pm} n_i^{\pm}$.

(6) A bound $E^{\pm}$ enzyme is detached from site i, with rate $k_\mathrm{d}^{\pm} n_i^{E^\pm}$.

APPENDIX B: LANGEVIN DYNAMICS

In this appendix we derive the Langevin equation for the total concentration field c by coarse-graining the stochastic process [Eqs. (1)–(3)]. This provides a pedagogical illustration of the methods used and recovers a standard result for diffusion processes [49]. Consider the total number of substrate molecules (+ species and − species) at site i, defined as $N_i = n_i^+ + n_i^-$. Let k_D be the microscopic hopping rate to any of the q neighboring sites on the lattice, where each d-dimensional site has volume Ω, and the center-to-center distance between neighboring sites is h. Within an infinitesimal time interval δt, we consider independent single events and calculate the probabilities for fluctuations to first order in δt:

$$\mathbb{P}[\delta N_i = +1] = \frac{k_D \delta t}{q} \sum_{j \in \mathcal{N}_i} N_j,$$

$$\mathbb{P}[\delta N_i = -1] = k_D \delta t N_i,$$

$$\mathbb{P}[\delta N_i = +1, \delta N_l = -1] = \frac{k_D \delta t}{q} \sum_{j \in \mathcal{N}_i} \delta_{j,l} N_l,$$

$$\mathbb{P}[\delta N_i = -1, \delta N_l = +1] = \frac{k_D \delta t}{q} \sum_{j \in \mathcal{N}_i} \delta_{j,l} N_i,$$

where $\mathcal{N}_i$ denotes the set of nearest neighbors of a site i on the lattice, and the final two expressions account for correlations between changes in neighboring sites due to molecular jumps.

From these equations, we calculate the first two moments of the fluctuations:

$$\mathbb{E}[\delta N_i] = \sum_v v\,\mathbb{P}[\delta N_i = v] = \frac{k_D\delta t}{q}\sum_{j\in\mathcal{N}_i}(N_j - N_i), \tag{B1}$$

$$\begin{aligned}\mathbb{E}[\delta N_i\delta N_l] &= \sum_{u,v} uv\mathbb{P}[\delta N_i = u, \delta N_l = v]\\ &= \frac{k_D\delta t}{q}\left[\delta_{i,l}\sum_{j\in\mathcal{N}_i}(N_j + N_i) - \sum_{j\in\mathcal{N}_i}\delta_{j,l}(N_j + N_i)\right].\end{aligned} \tag{B2}$$

To proceed to the continuum limit, we define the concentration field $N_i(t)/\Omega \to c(\vec{x}, t)$. Let $\hat{u}_k$ (for $k = 1, \dots, q$) be unit vectors pointing toward neighboring site centers. Lattice symmetry implies $\sum_k \hat{u}_k = 0$ and $\sum_k \hat{u}_{k,i}\hat{u}_{k,j} = q\,\delta_{i,j}/d$. Taking the continuum limit, where $\delta_{ij}/\Omega \to \delta(\vec{x}_i - \vec{x}_j)$ and $\frac{1}{q}\sum_{k=1}^{q}[c(\vec{x} + h\hat{u}_k, t) - c(\vec{x}, t)] \approx \frac{h^2}{2d}\nabla^2 c(\vec{x}, t)$, we define the macroscopic diffusion coefficient $D = \lim_{h\to 0}\frac{k_D h^2}{2d}$. The deterministic term becomes

$$\begin{aligned}\mathbb{E}[\delta c(\vec{x}, t)] &= \lim_{\Omega\to 0}\frac{\mathbb{E}[\delta N_i]}{\Omega} = \frac{k_D\delta t}{q}\\ &\times\sum_{k}^{q}[c(\vec{x} + h\hat{u}_k, t) - c(\vec{x}, t)] = D\delta t\nabla^2 c(\vec{x}, t).\end{aligned} \tag{B3}$$

The fluctuation term is derived analogously, yielding

$$\begin{aligned}\mathbb{E}[\delta c(\vec{x}, t)\delta c(\vec{x}', t)] &= \lim_{\Omega\to 0}\frac{\mathbb{E}[\delta N_i\delta N_l]}{\Omega^2}\\ &= 2D\delta t\,\nabla\cdot\nabla'[c(\vec{x}, t)\delta(\vec{x}' - \vec{x})].\end{aligned} \tag{B4}$$

This recovers the standard result [49]. The corresponding Langevin equation for the total concentration field c is therefore

$$\partial_t c(\vec{x}, t) = D\nabla^2 c + \nabla\cdot\vec{\zeta}_D, \tag{B5}$$

where $\vec{\zeta}_D$ is a zero-mean diffusion noise with correlation

$$\langle\zeta_D^i(\vec{x}, t)\zeta_D^j(\vec{x}', t')\rangle = 2Dc(\vec{x}, t)\delta_{i,j}\delta(\vec{x} - \vec{x}')\delta(t - t').$$

Due to the Markovian nature of the underlying microscopic process, Eq. (B5) must be interpreted in the Itô sense [49]. We thus obtain a self-consistent, purely diffusional dynamical equation for c. Note that the continuum limit should be regarded as a convenient notation. It implies a coarse-grained model where the size of a lattice site appears infinitesimal on the macroscopic scale, yet remains large enough to contain a sufficient number of molecules for a statistical description [49].

We now apply the same procedure to derive the Langevin equation for the order parameter field, ϕ, starting from the corresponding discrete field $n_i = n_i^+ - n_i^-$. Let $n_i^{E^\pm}$ be the number of $\pm$ enzymes at site i. The first two moments of δn_i are

$$\mathbb{E}[\delta n_i] = \left[\frac{2k_c^+ n_i^{E^+} n_i^-}{\gamma\Omega K_m^+ + n_i^-} + 2k_b^+ n_i^- - \frac{2k_c^- n_i^{E^-} n_i^+}{\gamma\Omega K_m^- + n_i^+} - 2k_b^- n_i^+ + \frac{k_D}{q}\sum_j(n_j - n_i)\right]\delta t,$$

$$\mathbb{E}[\delta n_i\delta n_l] = \left[\frac{4k_c^+ n_i^{E^+} n_i^-}{\gamma\Omega K_m^+ + n_i^-} + 4k_b^+ n_i^- - \frac{4k_c^- n_i^{E^-} n_i^+}{\gamma\Omega K_m^- + n_i^+} - 4k_b^- n_i^+ + \frac{k_D}{q}\sum_j(N_j + N_i)\right]\delta_{i,l}\,\delta t - \frac{k_D\delta t}{q}\sum_{j\in\mathcal{N}_i}\delta_{j,l}(N_j + N_i).$$

We define the continuum concentration fields: $n_i(t)/\Omega \to \phi(\vec{x}, t)$, $n_i^\pm(t)/\Omega \to \phi^\pm(\vec{x}, t)$, and$n_i^{E^\pm}(t)/\Omega \to E^\pm(\vec{x}, t)$. The first two moments for the fluctuations of the field ϕ are then calculated. Taking the continuum limit, they read

$$\mathbb{E}[\delta\phi(\vec{x}, t)] = \lim_{\Omega\to 0}\frac{\mathbb{E}[\delta n_i]}{\Omega} = \left(\frac{2k_c^+ E^+\phi^-}{\gamma K_m^+ + \phi^-} + 2k_b^+\phi^- - \frac{2k_c^- E^-\phi^+}{\gamma K_m^- + \phi^+} - 2k_b^-\phi^+ + D\nabla^2\phi\right)\delta t, \tag{B6}$$

$$\begin{aligned}\mathbb{E}[\delta\phi(\vec{x}, t)\delta\phi(\vec{x}', t)] &= \lim_{\Omega\to 0}\frac{\mathbb{E}[\delta n_i\delta n_l]}{\Omega} = \left(\frac{4k_c^+ E^+\phi^-}{\gamma K_m^+ + \phi^-} + 4k_b^+\phi^- + \frac{4k_c^- E^-\phi^+}{\gamma K_m^- + \phi^+} + 4k_b^-\phi^+\right)\delta(\vec{x} - \vec{x}')\,\delta t\\ &+ 2\delta t D\nabla\cdot\nabla'[c(\vec{x}, t)\delta(\vec{x}' - \vec{x})].\end{aligned} \tag{B7}$$

Given these moments, and using $\phi^\pm = (c \pm \phi)/2$ to reexpress the results in terms of c and ϕ, the Langevin equation for the order parameter field is [49]

$$\partial_t\phi(\vec{x}, t) = D\nabla^2\phi + A + \sqrt{B}\xi_R + \nabla\cdot\vec{\xi}_D, \tag{B8}$$

where

$$\begin{aligned}A &= \frac{2k_c^+ E^+(c - \phi)}{2\gamma K_m^+ + c - \phi} + k_b^+(c - \phi)\\ &- \frac{2k_c^- E^-(c + \phi)}{2\gamma K_m^- + c + \phi} - k_b^-(c + \phi),\end{aligned}$$

$$\begin{aligned}B &= \frac{4k_c^+ E^+(c - \phi)}{2\gamma K_m^+ + c - \phi} + 2k_b^+(c - \phi)\\ &+ \frac{4k_c^- E^-(c + \phi)}{2\gamma K_m^- + c + \phi} + 2k_b^-(c + \phi).\end{aligned}$$

Here, ξ_R and $\vec{\xi}_D$ are the zero-mean reactions and diffusion noise terms, respectively, with correlations

$$\langle\xi_R(\vec{x}, t)\xi_R(\vec{x}', t')\rangle = \delta(\vec{x} - \vec{x}')\delta(t - t'),$$

$$\langle\xi_D^i(\vec{x}, t)\xi_D^j(\vec{x}', t')\rangle = 2Dc(\vec{x}, t)\delta_{i,j}\delta(\vec{x} - \vec{x}')\delta(t - t').$$

By the same procedure we derive the Langevin equation for the enzymatic component,

$$\partial_t E^{\pm} = D\nabla^2 E^{\pm} + \frac{k_a^{\pm} E_f^{\pm}(c \pm \phi)}{2} - k_d^{\pm} E^{\pm} + \sqrt{\frac{k_a^{\pm} E_f^{\pm}(c \pm \phi)}{2} + k_d^{\pm} E^{\pm}}\, \eta_{E^{\pm}} + \nabla \cdot \vec{\eta}_{D^{\pm}}, \quad \text{(B9)}$$

where $\eta_{E^{\pm}}$ and $\vec{\eta}_{D^{\pm}}$ are the zero-mean reactions and diffusion noise terms, respectively, with correlations

$$\langle \eta_{E^{\pm}}(\vec{x}, t)\eta_{E^{\pm}}(\vec{x}', t')\rangle = \delta(\vec{x} - \vec{x}')\delta(t - t'),$$
$$\langle \eta^i_{D^{\pm}}(\vec{x}, t)\eta^j_{D^{\pm}}(\vec{x}', t')\rangle = 2DE^{\pm}(\vec{x}, t)\delta_{i,j}\delta(\vec{x} - \vec{x}')\delta(t - t'),$$

and for the reservoir concentration the following conservation law holds:

$$\partial_t E_f^{\pm} = -\frac{1}{\gamma}\langle \partial_t E^{\pm}\rangle_s, \quad \text{(B10)}$$

where $\langle \cdots \rangle_s$ denotes the spatial average over the scaffold.

The Langevin equations for the fields c, ϕ, and $E^{\pm}$ [Eqs. (B5), (B8), and (B9)] include diffusive noise terms. Since diffusive noise scales subdominantly with the coarse-graining length compared to nonconserved noise [79], these terms are neglected hereafter. Moreover, the total concentration c is unaffected by interconversion reactions and evolves through a purely diffusive process [Eq. (B5)]. After a relaxation transient, its average reaches a homogeneous value determined by the initial conditions. By neglecting the diffusive fluctuations around this mean, we can treat this field as a constant, $c(\vec{x}, t) = c$. Under this approximation, the dynamics of the substrate molecules on the scaffold is fully captured by the evolution of the order parameter field, $\phi(\vec{x}, t)$.

APPENDIX C: ADIABATIC ELIMINATION OF FAST VARIABLES

To simplify this set of coupled Langevin equations for the concentration difference ϕ and enzymes concentrations $E^{\pm}$ we perform an adiabatic elimination of fast variables. This allows us to enslave the enzyme degrees of freedom to the molecular concentrations. Specifically, we consider the regime where

$$k_D, k_c \ll k_d. \quad \text{(C1)}$$

Assuming for simplicity $k_d^{\pm} = k_d$, $k_c^{\pm} = k_c$, our system is described by three coupled Langevin equations:

$$\partial_t E^+ = k_d\left(\frac{D}{k_d}\nabla^2 E^+ + \bar{E}^+ - E^+\right) + \sqrt{k_d(\bar{E}^+ + E^+)}\eta_{E^+},$$
$$\partial_t E^- = k_d\left(\frac{D}{k_d}\nabla^2 E^- + \bar{E}^- - E^-\right) + \sqrt{k_d(\bar{E}^- + E^-)}\eta_{E^-},$$
$$\partial_t \phi = k_c f(\phi, E^{\pm}) + \sqrt{k_c\, g(\phi, E^{\pm})}\eta_{\phi}, \quad \text{(C2)}$$

where $\bar{E}^{\pm} = \frac{k_a^{\pm} E_f^{\pm}(c \pm \phi)}{2k_d^{\pm}}$ is the stationary value for the deterministic part of the equation for the enzymes, and f and g are defined by

$$f = \frac{D\nabla^2\phi + A}{k_c} = \frac{D}{k_c}\nabla^2\phi + \frac{2E^+(c - \phi)}{2\gamma K_m^+ + c - \phi} + \frac{k_b^+}{k_c}(c - \phi) - \frac{2E^-(c + \phi)}{2\gamma K_m^- + c + \phi} - \frac{k_b^-}{k_c}(c + \phi),$$
$$g = \frac{B}{k_c} = \frac{4E^+(c - \phi)}{2\gamma K_m^+ + c - \phi} + \frac{2k_b^+}{k_c}(c - \phi) + \frac{4E^-(c + \phi)}{2\gamma K_m^- + c + \phi} + \frac{2k_b^-}{k_c}(c + \phi),$$

where these terms are derived using the drift and variance from Eq. (B8), and the dependence on the rate k_c characterizing the timescale is made explicit. The noise has zero mean and correlation

$$\langle \eta_{\alpha}(t, \vec{x})\eta_{\beta}(t', \vec{x}')\rangle = \delta_{\alpha,\beta}\delta(t - t')\delta(\vec{x} - \vec{x}'). \quad \text{(C3)}$$

The diffusion terms in the equations for the enzymes can be neglected over scales $\lambda \gg \sqrt{\frac{k_D \Omega}{k_d}}$, which in the regime $k_D \ll k_d$ is below the resolution of the lattice. Moreover, when $k_d \gg k_c$, the field ϕ (and consequently $\bar{E}^{\pm}$) is slowly varying and we can approximate it as a constant on the characteristic timescale of the dynamics of $E^{\pm}$. Introducing the dimensionless time $s = k_c t$ and the dimensionless parameter $\epsilon = k_c/k_d$, we can rewrite the equations as

$$\partial_s E^+ = \epsilon^{-1}(\bar{E}^+ - E^+) + \sqrt{\epsilon^{-1}(\bar{E}^+ + E^+)}\tilde{\eta}_{E^+},$$
$$\partial_s E^- = \epsilon^{-1}(\bar{E}^- - E^-) + \sqrt{\epsilon^{-1}(\bar{E}^- + E^-)}\tilde{\eta}_{E^-},$$
$$\partial_s \phi = f(\phi, E^{\pm}) + \sqrt{g(\phi, E^{\pm})}\tilde{\eta}_{\phi}, \quad \text{(C4)}$$

where we rescale the noise $\tilde{\eta}_{\alpha} = \eta_{\alpha}/\sqrt{k_c}$ so that

$$\langle \tilde{\eta}_{\alpha}(t, \vec{x})\tilde{\eta}_{\beta}(t', \vec{x}')\rangle = \delta_{\alpha,\beta}\delta(t - t')\delta(\vec{x} - \vec{x}'). \quad \text{(C5)}$$

The dynamics of the enzymes is the faster one; therefore, $E^{\pm}$ rapidly relax to the stationary value $\bar{E}^{\pm}$. The stochastic process governing $E^{\pm}$ is a shifted Feller process, whose stationary distribution is a gamma distribution [49,80,81]. We can quantify the fluctuations $\delta E^{\pm}$ around the stationary value by expanding $E^{\pm}(s, \vec{x}) = \bar{E}^{\pm}(\vec{x}) + \delta E^{\pm}(s, \vec{x})$. When the local number of enzymes is large, fluctuations are small ($\delta E^{\pm} \ll \bar{E}^{\pm}$) and we can linearize the noise term by approximating $\sqrt{\bar{E}^{\pm} + \delta E^{\pm}} \approx \sqrt{\bar{E}^{\pm}}$. This way the process is reduced to a Gaussian Ornstein-Uhlenbeck process,

$$\partial_s \delta E^{\pm} = -\frac{1}{\epsilon}\delta E^{\pm} + \sqrt{\frac{2\bar{E}^{\pm}}{\epsilon}}\tilde{\eta}_{E^{\pm}}, \quad \text{(C6)}$$

with zero mean and correlation

$$\langle \delta E^{\pm}(s, \vec{x})\delta E^{\pm}(s', \vec{x}')\rangle = \bar{E}^{\pm}\delta(\vec{x} - \vec{x}')e^{-|s-s'|/\epsilon}. \quad \text{(C7)}$$

In the limit of small autocorrelation time ϵ, we can approximate the correlation by a δ function:

$$\langle \delta E^{\pm}(s, \vec{x})\delta E^{\pm}(s', \vec{x}')\rangle \xrightarrow{\epsilon \to 0} 2\epsilon\bar{E}^{\pm}\delta(\vec{x} - \vec{x}')\delta(s - s'). \quad \text{(C8)}$$

To study the effect of these small fluctuations on the slow dynamics of ϕ, we expand the function $f(\phi, E^{\pm})$ around

$E^{\pm} = \bar{E}^{\pm}$:

$$f(\phi, E^{\pm}) \approx f(\phi, \bar{E}^{\pm}) + \delta f(\phi, \bar{E}^{\pm}), \tag{C9}$$

where

$$\delta f = \partial_{E^+} f|_{E^+=\bar{E}^+}\, \delta E^+ + \partial_{E^-} f|_{E^-=\bar{E}^-}\, \delta E^- \tag{C10}$$

$$= \sqrt{2\epsilon \bar{E}^+}\, f_1^+(\phi)\tilde{\eta}_{E^+} + \sqrt{2\epsilon \bar{E}^-}\, f_1^-(\phi)\tilde{\eta}_{E^-}, \tag{C11}$$

and we define $f_1^+(\phi) = \partial_{E^+} f(\phi, E^{\pm})|_{E^{\pm}=\bar{E}^{\pm}}$, $f_1^-(\phi) = \partial_{E^-} f(\phi, E^{\pm})|_{E^{\pm}=\bar{E}^{\pm}}$. At leading order, once we neglect cross-correlations between noise terms in the dynamics of molecules and enzymes, we can approximate $g(\phi, E^{\pm}) \approx g(\phi, \bar{E}^{\pm})$. The equation for ϕ can be rewritten as

$$\partial_s \phi = f(\phi, \bar{E}^{\pm}) + \xi \tag{C12}$$

with

$$\langle \xi(s, \vec{x})\xi(s', \vec{x}')\rangle = \{g(\phi, \bar{E}^{\pm}) + 2\epsilon[\bar{E}^+ f_1^+(\phi)^2 + \bar{E}^- f_1^-(\phi)^2]\}\delta(\vec{x} - \vec{x}')\delta(s - s').$$

Switching back to the original timescale, the equation for the slow variable ϕ reads

$$\partial_t \phi = D\nabla^2\phi + A + \sqrt{B}\,\eta \tag{C13}$$

with A and B given by

$$A = \frac{2k_c \bar{E}^+(c - \phi)}{2\gamma K_m^+ + c - \phi} + k_b^+(c - \phi) - \frac{2k_c \bar{E}^-(c + \phi)}{2\gamma K_m^- + c + \phi} - k_b^-(c + \phi), \tag{C14}$$

$$B = \frac{4k_c \bar{E}^+(c - \phi)}{2\gamma K_m^+ + c - \phi}\left(1 + 2\epsilon\frac{c - \phi}{2\gamma K_m^+ + c - \phi}\right) + \frac{4k_c \bar{E}^-(c + \phi)}{2\gamma K_m^- + c + \phi}\left(1 + 2\epsilon\frac{c + \phi}{2\gamma K_m^- + c + \phi}\right) + 2k_b^+(c - \phi) + 2k_b^-(c + \phi), \tag{C15}$$

and η a zero-mean noise with correlation

$$\langle \eta(\vec{x}, t)\eta(\vec{x}', t')\rangle = \delta(\vec{x} - \vec{x}')\delta(t - t').$$

As a result of the adiabatic elimination of the enzyme degrees of freedom, the noise amplitude in Eq. (C15) now contains additional $\mathcal{O}(\epsilon)$ terms that are not present in the intrinsic noise of the field ϕ [cf. Eq. (B8)]. These corrections have a functional form similar to the intrinsic noise of ϕ and thus effectively result in a small renormalization of the noise strength. Since simulations are performed in a parameter regime where $\epsilon \lesssim 1$, these corrections are neglected hereafter to maintain analytical tractability.

In the expression for the stationary concentration of the enzymes, $\bar{E}^{\pm} = \frac{k_a^{\pm} E_f^{\pm}(c \pm \phi)}{2k_d^{\pm}}$, in the fast-shuttling regime we can substitute the cytosolic concentration $E_f^{\pm}$ with its stationary value, $E_f^{\pm} = \frac{2\gamma K_d^{\pm} E_{tot}^{\pm}}{2\gamma K_d^{\pm} + c \pm \langle\phi\rangle_s}$, where $K_d^{\pm} = k_d^{\pm}/k_a^{\pm}$.

With these assumptions, we reduce the system's description to a single stochastic equation for the order parameter ϕ, given by Eq. (7) in the main text. For convenience, we provide a summary of the symbols used for the relevant fields and parameters of the theory in Tables I and II.

APPENDIX D: PHASE DIAGRAM

The effective catalytic ratio $\rho = k_e^+/k_e^-$ can be determined as a function of the field average $\langle\phi\rangle_s$:

$$\rho = \frac{2\gamma K_d^- + c - \langle\phi\rangle_s}{2\gamma K_d^+ + c + \langle\phi\rangle_s}\,\rho_0, \tag{D1}$$

where

$$\rho_0 = \frac{k_c^+ E_{tot}^+}{k_c^- E_{tot}^-}.$$

Since the field average is constrained by $-c \leqslant \langle\phi\rangle_s \leqslant c$, the values of ρ must lie in the physical region defined by

$$\frac{\rho_0}{\rho_+} \leqslant \rho \leqslant \frac{\rho_0}{\rho_-}, \tag{D2}$$

where

$$\rho_+ = \frac{K_d^+ + C}{K_d^-}, \quad \rho_- = \frac{K_d^+}{K_d^- + C}. \tag{D3}$$

The physically accessible values of ρ are thus controlled by the rates of enzyme shuttling to and from the cytosol. At each instant in time, the system's state is characterized by a value of ρ inside the physical region bounded by the solid curves in Fig. 2 (corresponding to $\langle\phi\rangle_s = \pm c$). The parameter ρ_0 controls the center of this region, while K_d/C controls its width. Let us assume now that $\rho > 1$, so that the + phase is favored. The average value of the field $\langle\phi\rangle$ slowly increases in time due to the expansion of the + phase. This increase, in turn, leads to a decrease in ρ [see Eq. (D1)]. By the same reasoning, we find that for $\rho < 1$, the dynamics causes ρ to increase. In other words, the global feedback mechanism always drives the system toward $\rho = 1$ and, if this state is accessible, the system asymptotically reaches it.

From this dynamical picture, it is possible to extract information that is independent of the system's specific trajectory. From Eq. (19), it follows that the phase-coexistence line $\rho = 1$ is reachable and, therefore, the system can relax in the steady state of phase coexistence, if the condition

$$\rho_- \leqslant \rho_0 \leqslant \rho_+ \tag{D4}$$

is satisfied. This finding allows us to explicitly draw the steady-state phase diagram of the system, shown in Fig. 3(a). The width of the phase-coexistence region on a logarithmic scale is characterized by the ratio

$$\frac{\rho_+}{\rho_-} = \left(1 + \frac{C}{K_d^+}\right)\left(1 + \frac{C}{K_d^-}\right). \tag{D5}$$

The region of parameters for which phase coexistence is observed is thus controlled by the dissociation constants.

Inverting Eq. (D1), we obtain the average value of the field $\langle\phi\rangle_s$ at steady state,

$$\langle\phi\rangle_s = \frac{(1 + 2K_d^-/C)\rho_0 - (1 + 2K_d^+/C)\rho}{\rho_0 + \rho}\,c, \tag{D6}$$

and the membrane fraction occupied by each of the ± phases,

$$\langle\phi_\pm\rangle_s = \frac{1 + K_\mp^d/C - (\rho/\rho_0)^{\pm 1} K_\pm^d/C}{1 + (\rho/\rho_0)^{\pm 1}}\,c. \tag{D7}$$

The steady-state, phase-coexistence values [Eq. (23)] are obtained by substituting $\rho = 1$ into the expressions above.

APPENDIX E: POLYNOMIAL APPROXIMATION

The effective catalytic potential (17) for $k_b^\pm = k_b$ and $K_m^\pm = K_m$ is well approximated by the polynomial expression

$$\tilde{V}(\phi) = \frac{a}{4}(c^2 - \phi^2)^2 + a\phi_0\left(c^2 - \frac{1}{3}\phi^2\right)\phi + k_b\phi^2, \tag{E1}$$

where

$$a = 2\,\frac{k_e^+ + k_e^-}{c^2} g(K_m/C), \tag{E2}$$

$$g(\kappa) = 1 + 4\kappa(1+\kappa)\ln\frac{4\kappa(1+\kappa)}{(1+2\kappa)^2}, \tag{E3}$$

$$\phi_0 = (1 + 2K_m/C)\frac{k_e^+ - k_e^-}{k_e^+ + k_e^-}\,c. \tag{E4}$$

For $k_b = 0$ and $\phi_0 = 0$, approximation (E1) has the same critical points and potential barrier between the two wells as the original potential (17). The function $g(\kappa)$ is monotonically decreasing, with $g(\kappa) \sim 1 + 4\kappa\ln(4\kappa)$ for small κ, and $g(\kappa) \sim 1/(8\kappa^2)$ for large κ.

Differentiating the approximated potential (E1) yields the following approximation for the deterministic drift:

$$\tilde{A} = 2(k_e^+ + k_e^-)g(K_m/C)(1 - \phi^2/c^2)(\phi - \phi_0) - 2k_b\phi = 2(\tilde{R}^+ - \tilde{R}^-). \tag{E5}$$

This expression is given in terms of polynomial approximations for the reaction terms:

$$\tilde{R}^\pm = k_e^\pm g(K_m/C)(1 - \phi^2/c^2)(c + 2K_m/\gamma \pm \phi) \mp \frac{k_b}{2}\phi. \tag{E6}$$

From these expressions, a polynomial approximation $\tilde{B}$ for the noise term is readily obtained:

$$\tilde{B} = 4(\tilde{R}^+ + \tilde{R}^-) = 4(k_e^+ + k_e^-)g(K_m/C)(1 - \phi^2/c^2) \times \left(c + 2K_m/\gamma + \frac{k_e^+ - k_e^-}{k_e^+ + k_e^-}\phi\right) + 4k_b\phi. \tag{E7}$$

APPENDIX F: DROPLET NUCLEATION

We consider the nucleation of a circular droplet of the metastable phase within a homogeneous sea of the less-stable phase, in a d-dimensional space. We adopt a radial droplet ansatz $\phi(\vec{x}, t) = \phi((r - R(t))/w)$, where $r = |\vec{x}|$, $R(t)$ is the droplet radius, and w is the interfacial width. Along the optimal nucleation path, the droplet growth is monotonic. This makes the mapping $t \mapsto R(t)$ invertible, allowing us to use R as the evolution parameter instead of time. Substituting this ansatz into the action (32) gives

$$S = 2S_d\int_0^R \mathrm{d}R'\int_0^\infty \mathrm{d}r\left\{r^{d-1}\frac{A[\phi] + D\left(\frac{d-1}{wr}\phi' + \frac{1}{w^2}\phi''\right)}{B[\phi]}\,\frac{\phi'}{w}\right\}, \tag{F1}$$

where S_d is the solid angle in d dimensions. Switching to the variable $z = (r - R')/w$, we get

$$S = 2S_d\int_0^R \mathrm{d}R'\int_{-R'/w}^\infty \mathrm{d}z\left\{\frac{\phi'(zw + R')^{d-1}}{B[\phi]}\left(A[\phi] + \frac{D(d-1)}{(zw+R')w}\phi' + \frac{D}{w^2}\phi''\right)\right\}, \tag{F2}$$

where the profile ϕ and its derivatives ϕ' and ϕ'', are evaluated at z. The three terms of the action are computed in the thin-wall approximation, which assumes that ϕ' is sharply peaked at the interface and zero elsewhere. The first term is

$$2S_d\int_0^R \mathrm{d}R'\int_{-R'/w}^\infty \mathrm{d}z\left\{\frac{\phi'(zw + R')^{d-1}A[\phi]}{B[\phi]}\right\} \approx 2S_d\int_0^R \mathrm{d}R'R'^{d-1}\int_{-R'/w}^\infty \frac{\phi' A[\phi]}{B[\phi]}\mathrm{d}z \approx 2\frac{S_d}{d}R^d\int_{\phi_s}^{\phi_m}\frac{A[\phi]}{B[\phi]}\mathrm{d}\phi, \tag{F3}$$

where the extrema ϕ_m and ϕ_s are the values of the field in the metastable and stable phases, respectively. Similarly, the second term reads

$$2S_d\int_0^R \mathrm{d}R'\frac{D(d-1)}{w}\int_{-R'/w}^\infty \mathrm{d}z\left\{(zw + R')^{d-2}\frac{(\phi')^2}{B[\phi]}\right\} \approx 2S_d D R^{d-1}\int_{\phi_s}^{\phi_m}\frac{\phi'}{B(\phi)}\mathrm{d}\phi. \tag{F4}$$

For the remaining contribution, integrating by parts and using the thin-wall approximation to neglect boundary terms, we get

$$2S_d\int_0^R \mathrm{d}R' D\int_{-R'/w}^\infty \mathrm{d}z\left\{\frac{(zw + R')^{d-1}}{w^2 B(\phi)}\frac{\mathrm{d}}{\mathrm{d}z}\left[\frac{1}{2}(\phi')^2\right]\right\} \tag{F5}$$

$$\approx -2S_d\int_0^R \mathrm{d}R' D\int_{-R'/w}^\infty \mathrm{d}z\left\{\frac{\mathrm{d}}{\mathrm{d}z}\left[\frac{(zw + R')^{d-1}}{w^2 B(\phi)}\right]\frac{1}{2}(\phi')^2\right\} \tag{F6}$$

$$\approx -S_d D R^{d-1}\int_{\phi_s}^{\phi_m}\frac{\phi'}{B(\phi)}\mathrm{d}\phi + S_d D\frac{R^d}{d}\int_{\phi_s}^{\phi_m}\frac{\phi'^2 B'(\phi)}{B^2(\phi)}. \tag{F7}$$

Combining the above contributions, the action for the formation of a droplet of radius R starting from a metastable homogeneous state is

$$S = 2S_d\left[R^{d-1}I_1 - \frac{R^d}{d}(\Delta\tilde{V} - I_2)\right], \tag{F8}$$

where the coefficients are defined as

$$I_1 = \frac{D}{2}\int_{\phi_s}^{\phi_m}\frac{\phi'}{B(\phi)}\mathrm{d}\phi, \tag{F9}$$

$$\Delta\tilde{V} = -\int_{\phi_s}^{\phi_m}\frac{A(\phi)}{B(\phi)}\mathrm{d}\phi, \tag{F10}$$

$$I_2 = \frac{D}{2}\int_{\phi_s}^{\phi_m}\frac{\phi'^2 B'(\phi)}{B^2(\phi)}\mathrm{d}\phi. \tag{F11}$$

The critical radius is finally found by maximizing the action (F8) with respect to R:

$$R_c = \frac{(d-1)I_1}{\Delta\tilde{V} - I_2}. \tag{F12}$$

It is worth noticing here that in the limit of additive noise (i.e., $B = \text{const}$), this result reduces to the well-known expression from classical nucleation theory.

The action in Eq. (F8) is valid to describe the nucleation event, while the dynamics of a domain of size much greater than R_c is mainly deterministic. The integrals in Eqs. (F9)–(F11) can be evaluated for $K_m^\pm = K_m$ and $k_b^\pm = k_b$ using the polynomial approximations for the drift and noise terms provided in Appendix E, and the fact that, near phase coexistence, $\phi' \simeq [\frac{2}{D}V(\phi)]^{1/2}$. As a result, for vanishing anisotropy and basal interconversion ($\phi_0 \to 0$, $k_b \to 0$), we obtain

$$R_c = \frac{\sqrt{D(k_e^+ + k_e^-)}}{4\,|k_e^+ - k_e^-|\left(1 + \frac{2K_m}{C} + \frac{2/3}{1+\frac{2K_m}{C}}\right)\sqrt{g\left(\frac{K_m}{C}\right)}}. \tag{F13}$$

In general, Eq. (F13) is an implicit equation for R_c, since the rates $k_e^\pm$ depend on the average field $\langle\phi\rangle$ through Eq. (11). However, this dependence is negligible when a single domain of radius $R \ll s$ is present, where s is the linear size of the system. For the theoretical curve in Fig. 9, we account for this dependence by assuming $\langle\phi\rangle_s/c = \frac{2\pi R^2}{s^2} - 1$ and numerically solving the coupled system given by Eqs. (11) and (F13) for R_c.

APPENDIX G: NUMERICAL METHOD

To efficiently simulate the stochastic dynamics described in Appendix A, we develop an *ad hoc* code for a Gillespie-like [82] algorithm in the julia language [78]. For efficient event sampling with dynamically changing rates, we employ a variant of Algorithms 6 and 7 from Ref. [83]. In short, this technique makes use of a binary tree to store event rates and their partial sums, guaranteeing just $O(\log N)$ time and two pseudorandom number extractions per Gillespie jump, where N is the number of possible events. This scheme allows to efficiently implement reaction and diffusion rates that depend on the number of molecules in the reservoir (in addition to the number of molecules at each site), even when a change in the reservoir affects an extensive number of event rates.

For all simulations, we consider a system of linear size $L = 100$ and $\gamma = 10$, which corresponds to a reservoir volume of $L^2\gamma$. Parameters used in the simulations are reported in Table III.

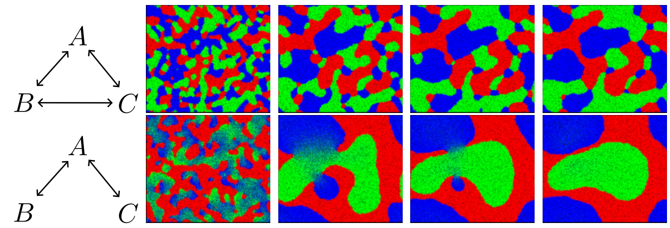

FIG. 11. Examples of three-way phase separation in an abstract system with six reactions $E^{xy} + x \to E^{xy} + y$ for $x, y \in \{A = \text{red}, B = \text{blue}, C = \text{green}\}$, $x \neq y$. The diffusion rate is $k_D = 0.1$ for all species, and $\gamma K_m = 1$ for all reactions. Top: Symmetric phase separation; all reaction constants are $k_c^{xy} = 1$. Bottom: Asymmetric phase separation, $k_c^{AB} = k_c^{AC} = 0.8$, $k_c^{BA} = k_c^{CA} = 1$, and $k_c^{BC} = k_c^{CB} = 0$.

APPENDIX H: MULTIPLE SPECIES

The model can be easily extended to describe the activity of several modules working in parallel. As an example, consider the following abstract system of three molecular species A, B, C, with reactions catalyzed by six enzymes E^{xy}, where $x, y \in \{A, B, C\}$ and $x \neq y$:

$$E^{xy} + x \xrightarrow{k_c^{xy}} E^{xy} + y,$$

resulting in a three-way process of phase separation. An example of the evolution of such a system under symmetric conditions for the three molecules is shown in Fig. 11 (top row). When $k_c^{BC} = k_c^{CB} = 0$ (resulting in just four effective reactions), a direct interface between molecules B and C is disfavored, and this interface is typically interposed with molecule A (see Fig. 11, bottom row).

[1] B. Alberts, R. Heald, A. Johnson, D. Morgan, M. Raff, K. Roberts, and P. Walter, *Molecular Biology of the Cell*, 7th ed. (W.W. Norton, New York, 2022).

[2] A. A. Hyman, C. A. Weber, and F. Jülicher, Liquid-liquid phase separation in biology, Annu. Rev. Cell Dev. Biol. **30**, 39 (2014).

[3] S. F. Banani, H. O. Lee, A. A. Hyman, and M. K. Rosen, Biomolecular condensates: Organizers of cellular biochemistry, Nat. Rev. Mol. Cell Biol. **18**, 285 (2017).

[4] X. Fang, K. Kruse, T. Lu, and J. Wang, Nonequilibrium physics in biology, Rev. Mod. Phys. **91**, 045004 (2019).

[5] A. Musacchio, On the role of phase separation in the biogenesis of membraneless compartments, EMBO J. **41**, EMBJ2021109952 (2022).

[6] M. E. Cates and C. Nardini, Active phase separation: New phenomenology from non-equilibrium physics, Rep. Prog. Phys. **88**, 056601 (2025).

[7] D. Zwicker, A. A. Hyman, and F. Jülicher, Suppression of Ostwald ripening in active emulsions, Phys. Rev. E **92**, 012317 (2015).
[8] F. Brauns, H. Weyer, J. Halatek, J. Yoon, and E. Frey, Wavelength selection by interrupted coarsening in reaction-diffusion systems, Phys. Rev. Lett. **126**, 104101 (2021).
[9] C. A. Weber, D. Zwicker, F. Jülicher, and C. F. Lee, Physics of active emulsions, Rep. Prog. Phys. **82**, 064601 (2019).
[10] V. T. Yan, A. Narayanan, T. Wiegand, F. Jülicher, and S. W. Grill, A condensate dynamic instability orchestrates actomyosin cortex activation, Nature (London) **609**, 597 (2022).
[11] J. Bauermann, G. Bartolucci, C. A. Weber, and F. Jülicher, Theory of reversed ripening in active phase separating systems, Phys. Rev. Lett. **135**, 148201 (2025).
[12] A. Das, A. Polley, and M. Rao, Phase segregation of passive advective particles in an active medium, Phys. Rev. Lett. **116**, 068306 (2016).
[13] M. W. Cotton, R. Golestanian, and J. Agudo-Canalejo, Catalysis-induced phase separation and autoregulation of enzymatic activity, Phys. Rev. Lett. **129**, 158101 (2022).
[14] S. Saha, A. Das, C. Patra, A. A. Anilkumar, P. Sil, S. Mayor, and M. Rao, Active emulsions in living cell membranes driven by contractile stresses and transbilayer coupling, Proc. Natl. Acad. Sci. USA **119**, e2123056119 (2022).
[15] T. Burkart, M. C. Wigbers, L. Würthner, and E. Frey, Control of protein-based pattern formation via guiding cues, Nat. Rev. Phys. **4**, 511 (2022).
[16] M. E. Cates and C. Nardini, Classical nucleation theory for active fluid phase separation, Phys. Rev. Lett. **130**, 098203 (2023).
[17] N. Ziethen, J. Kirschbaum, and D. Zwicker, Nucleation of chemically active droplets, Phys. Rev. Lett. **130**, 248201 (2023).
[18] L. Demarchi, A. Goychuk, I. Maryshev, and E. Frey, Enzyme-enriched condensates show self-propulsion, positioning, and coexistence, Phys. Rev. Lett. **130**, 128401 (2023).
[19] Y. Zhang, A. Manacorda, and É. Fodor, Species interconversion of deformable particles yields transient phase separation, New J. Phys. **27**, 043023 (2025).
[20] Y. Cho and W. M. Jacobs, Interfacial effects determine nonequilibrium phase behaviors in chemically driven fluids, Proc. Natl. Acad. Sci. USA **122**, e2501145122 (2025).
[21] S. D. Hansen, W. Y. Huang, Y. K. Lee, P. Bieling, S. M. Christensen, and J. T. Groves, Stochastic geometry sensing and polarization in a lipid kinase–phosphatase competitive reaction, Proc. Natl. Acad. Sci. USA **116**, 15013 (2019).
[22] A. A. Lee, W. Y. Huang, S. D. Hansen, N. H. Kim, S. Alvarez, and J. T. Groves, Stochasticity and positive feedback enable enzyme kinetics at the membrane to sense reaction size, Proc. Natl. Acad. Sci. USA **118**, e2103626118 (2021).
[23] A. Cezanne, J. Lauer, A. Solomatina, I. F. Sbalzarini, and M. Zerial, A non-linear system patterns Rab5 GTPase on the membrane, eLife **9**, e54434 (2020).
[24] A. Gamba, A. de Candia, S. Di Talia, A. Coniglio, F. Bussolino, and G. Serini, Diffusion-limited phase separation in eukaryotic chemotaxis, Proc. Natl. Acad. Sci. USA **102**, 16927 (2005) (see in particular the mass-conserving reaction-diffusion model described in the supporting text).
[25] A. Gamba, I. Kolokolov, V. Lebedev, and G. Ortenzi, Patch coalescence as a mechanism for eukaryotic directional sensing, Phys. Rev. Lett. **99**, 158101 (2007).
[26] M. Otsuji, S. Ishihara, C. Co, K. Kaibuchi, A. Mochizuki, and S. Kuroda, A mass conserved reaction–diffusion system captures properties of cell polarity, PLoS Comput. Biol. **3**, e108 (2007).
[27] J. Halatek and E. Frey, Rethinking pattern formation in reaction–diffusion systems, Nat. Phys. **14**, 507 (2018).
[28] J. Halatek, F. Brauns, and E. Frey, Self-organization principles of intracellular pattern formation, Philos. Trans. R. Soc. B **373**, 20170107 (2018).
[29] F. Brauns, J. Halatek, and E. Frey, Phase-space geometry of mass-conserving reaction-diffusion dynamics, Phys. Rev. X **10**, 041036 (2020).
[30] P. C. Hohenberg and B. I. Halperin, Theory of dynamic critical phenomena, Rev. Mod. Phys. **49**, 435 (1977).
[31] C. Sire and S. N. Majumdar, Coarsening in the q-state Potts model and the Ising model with globally conserved magnetization, Phys. Rev. E **52**, 244 (1995).
[32] F. Schlögl, Chemical reaction models for non-equilibrium phase transitions, Z. Phys. **253**, 147 (1972).
[33] A. Goldbeter and D. E. Koshland, Jr., An amplified sensitivity arising from covalent modification in biological systems., Proc. Natl. Acad. Sci. USA **78**, 6840 (1981).
[34] A. J. Bray, Theory of phase-ordering kinetics, Adv. Phys. **43**, 357 (1994).
[35] A. Gamba, I. Kolokolov, V. Lebedev, and G. Ortenzi, Universal features of cell polarization processes, J. Stat. Mech. (2009) P02019.
[36] M. Semplice, A. Veglio, G. Naldi, G. Serini, and A. Gamba, A bistable model of cell polarity, PLoS One **7**, e30977 (2012).
[37] A. Veglio, A. Gamba, M. Nicodemi, F. Bussolino, and G. Serini, Symmetry breaking mechanism for epithelial cell polarization, Phys. Rev. E **80**, 031919 (2009).
[38] K. Kruse, A dynamic model for determining the middle of *Escherichia coli*, Biophys. J. **82**, 618 (2002).
[39] G. Meacci and K. Kruse, Min-oscillations in *Escherichia coli* induced by interactions of membrane-bound proteins, Phys. Biol. **2**, 89 (2005).
[40] K. C. Huang, Y. Meir, and N. S. Wingreen, Dynamic structures in *Escherichia coli*: Spontaneous formation of MinE rings and MinD polar zones, Proc. Natl. Acad. Sci. USA **100**, 12724 (2003).
[41] M. Zamparo, F. Chianale, C. Tebaldi, M. Cosentino-Lagomarsino, M. Nicodemi, and A. Gamba, Dynamic membrane patterning, signal localization and polarity in living cells, Soft Matter **11**, 838 (2015).
[42] H. Weyer, F. Brauns, and E. Frey, Coarsening and wavelength selection far from equilibrium: A unifying framework based on singular perturbation theory, Phys. Rev. E **108**, 064202 (2023).
[43] J. F. Robinson, T. Machon, and T. Speck, Universal limiting behavior of reaction-diffusion systems with conservation laws, Phys. Rev. E **111**, 065417 (2025).
[44] R. Wittkowski, A. Tiribocchi, J. Stenhammar, R. J. Allen, D. Marenduzzo, and M. E. Cates, Scalar $\varphi 4$ field theory for active-particle phase separation, Nat. Commun. **5**, 4351 (2014).
[45] M. E. Cates and J. Tailleur, Motility-induced phase separation, Annu. Rev. Condens. Matter Phys. **6**, 219 (2015).
[46] S. Bureković, F. D. Luca, M. E. Cates, and C. Nardini, Active Cahn-Hilliard theory for non-equilibrium phase separation: Quantitative macroscopic predictions and a microscopic derivation, arXiv:2601.16539.

[47] N. R. Leslie, R. M. Biondi, and D. R. Alessi, Phosphoinositide-regulated kinases and phosphoinositide phosphatases, Chem. Rev. **101**, 2365 (2001).

[48] C. B. Marshall, D. Meiri, M. J. Smith, M. T. Mazhab-Jafari, G. M. Gasmi-Seabrook, R. Rottapel, V. Stambolic, and M. Ikura, Probing the GTPase cycle with real-time NMR: GAP and GEF activities in cell extracts, Methods **57**, 473 (2012).

[49] C. W. Gardiner, *Handbook of Stochastic Methods for Physics, Chemistry and the Natural Sciences* (Springer, Berlin, 1985).

[50] Y. Mori, A. Jilkine, and L. Edelstein-Keshet, Wave-pinning and cell polarity from a bistable reaction-diffusion system, Biophys. J. **94**, 3684 (2008).

[51] P. C. Martin, E. D. Siggia, and H. A. Rose, Statistical dynamics of classical systems, Phys. Rev. A **8**, 423 (1973).

[52] A. Kamenev, *Field Theory of Non-equilibrium Systems* (Cambridge University Press, Cambridge, UK, 2023).

[53] A. Ridley, M. Schwartz, K. Burridge, R. Firtel, M. Ginsberg, G. Borisy, J. Parsons, and A. Horwitz, Cell migration: Integrating signals from front to back, Science **302**, 1704 (2003).

[54] V. Kolösch, P. G. Charest, and R. A. Firtel, The regulation of cell motility and chemotaxis by phospholipid signaling, J. Cell Sci. **121**, 551 (2008).

[55] C. R. Cowan and A. A. Hyman, Asymmetric cell division in *C. elegans*: Cortical polarity and spindle positioning, Annu. Rev. Cell Dev. Biol. **20**, 427 (2004).

[56] Z. G. Venkei and Y. M. Yamashita, Emerging mechanisms of asymmetric stem cell division, J. Cell Biol. **217**, 3785 (2018).

[57] A. S. Howell, M. Jin, C.-F. Wu, T. R. Zyla, T. C. Elston, and D. J. Lew, Negative feedback enhances robustness in the yeast polarity establishment circuit, Cell **149**, 322 (2012).

[58] C.-F. Wu, J.-G. Chiou, M. Minakova, B. Woods, D. Tsygankov, T. R. Zyla, N. S. Savage, T. C. Elston, and D. J. Lew, Role of competition between polarity sites in establishing a unique front, eLife **4**, e11611 (2015).

[59] M. F. Krummel and I. Macara, Maintenance and modulation of T cell polarity, Nat. Immunol. **7**, 1143 (2006).

[60] M. B. Stone, S. A. Shelby, M. F. Núñez, K. Wisser, and S. L. Veatch, Protein sorting by lipid phase-like domains supports emergent signaling function in B lymphocyte plasma membranes, eLife **6**, e19891 (2017).

[61] K. J. Day, G. Kago, L. Wang, J. B. Richter, C. C. Hayden, E. M. Lafer, and J. C. Stachowiak, Liquid-like protein interactions catalyse assembly of endocytic vesicles, Nat. Cell Biol. **23**, 366 (2021).

[62] M. Zamparo, D. Valdembri, G. Serini, I. V. Kolokolov, V. V. Lebedev, L. Dall'Asta, and A. Gamba, Optimality in self-organized molecular sorting, Phys. Rev. Lett. **126**, 088101 (2021).

[63] R. Wedlich-Soldner and R. Li, Spontaneous cell polarization: Undermining determinism, Nat. Cell Biol. **5**, 267 (2003).

[64] M. I. Freidlin and A. D. Wentzell, Random perturbations, in *Random Perturbations of Dynamical Systems* (Springer, Berlin, 1998), pp. 15–43.

[65] H. Touchette, The large deviation approach to statistical mechanics, Phys. Rep. **478**, 1 (2009).

[66] A. Vulpiani, F. Cecconi, M. Cencini, A. Puglisi, and D. Vergni, *Large Deviations in Physics: The Legacy of the Law of Large Numbers* (Springer, Berlin, 2014).

[67] T. M. Liggett, Coexistence in threshold voter models, Ann. Probab. **22**, 764 (1994).

[68] E. Ben-Naim, L. Frachebourg, and P. L. Krapivsky, Coarsening and persistence in the voter model, Phys. Rev. E **53**, 3078 (1996).

[69] C. Castellano, M. A. Muñoz, and R. Pastor-Satorras, Nonlinear q-voter model, Phys. Rev. E **80**, 041129 (2009).

[70] F. Schweitzer and L. Behera, Nonlinear voter models: The transition from invasion to coexistence, Eur. Phys. J. B **67**, 301 (2009).

[71] L. C. F. Latoski, W. G. Dantas, and J. J. Arenzon, Curvature-driven growth and interfacial noise in the voter model with self-induced zealots, Phys. Rev. E **106**, 014121 (2022).

[72] E. Floris, A. Piras, F. S. Pezzicoli, M. Zamparo, L. Dall'Asta, and A. Gamba, Phase separation and critical size in molecular sorting, Phys. Rev. E **106**, 044412 (2022).

[73] M. Chatzittofi, N. Ziethen, C. Nardini, and M. E. Cates, Nonequilibrium nucleation theory for nonconserved fields: From active matter to population dynamics, arXiv:2606.18911.

[74] J. E. Ferrell, Jr., and E. M. Machleder, The biochemical basis of an all-or-none cell fate switch in *Xenopus* oocytes, Science **280**, 895 (1998).

[75] M. Nicodemi and A. Prisco, Thermodynamic pathways to genome spatial organization in the cell nucleus, Biophys. J. **96**, 2168 (2009).

[76] Z. Feng, X. Chen, X. Wu, and M. Zhang, Formation of biological condensates via phase separation: Characteristics, analytical methods, and physiological implications, J. Biol. Chem. **294**, 14823 (2019).

[77] S. Matsuoka, T. Shibata, and M. Ueda, Asymmetric PTEN distribution regulated by spatial heterogeneity in membrane-binding state transitions, PLoS Comput. Biol. **9**, e1002862 (2013).

[78] D. Andreghetti, A. Braunstein, L. Dall'Asta, and A. Gamba, MembraneRD.jl, 2025, https://github.com/damiano-andreghetti/MembraneRD.jl.

[79] K. J. Wiese, Coherent-state path integral versus coarse-grained effective stochastic equation of motion: From reaction diffusion to stochastic sandpiles, Phys. Rev. E **93**, 042117 (2016).

[80] W. Feller, Two singular diffusion problems, Ann. Math. **54**, 173 (1951).

[81] J. C. Cox, J. E. Ingersoll, and S. A. Ross, A theory of the term structure of interest rates, Econometrica **53**, 385 (1985).

[82] D. T. Gillespie, Exact stochastic simulation of coupled chemical reactions, J. Phys. Chem. **81**, 2340 (1977).

[83] V. H. Thanh, R. Zunino, and C. Priami, Efficient constant-time complexity algorithm for stochastic simulation of large reaction networks, IEEE/ACM Trans. Comput. Biol. Bioinf. **14**, 657 (2016).